Wind-Driven Circulation in a Shelf Valley. Part II: Dynamics of the Along-Valley Velocity and Transport

WEIFENG (GORDON) ZHANG

Applied Ocean Physics and Engineering Department, Woods Hole Oceanographic Institution, Woods Hole, Massachusetts

STEVEN J. LENTZ

Physical Oceanography Department, Woods Hole Oceanographic Institution, Woods Hole, Massachusetts

(Manuscript received 25 April 2017, in final form 23 February 2018)

ABSTRACT

The dynamics controlling the along-valley (cross shelf) flow in idealized shallow shelf valleys with small to moderate Burger number are investigated, and analytical scales of the along-valley flows are derived. This paper follows Part I, which shows that along-shelf winds in the opposite direction to coastal-trapped wave propagation (upwelling regime) force a strong up-valley flow caused by the formation of a lee wave. In contrast, along-shelf winds in the other direction (downwelling regime) do not generate a lee wave and consequently force a relatively weak net down-valley flow. The valley flows in both regimes are cyclostrophic with $O(1)$ Rossby number. A major difference between the two regimes is the along-shelf length scales of the along-valley flows L_x. In the upwelling regime L_x depends on the valley width W_c and the wavelength λ_{lw} of the coastal-trapped lee wave arrested by the along-shelf flow U_s. In the downwelling regime L_x depends on the inertial length scale $|U_s|/f$ and W_c. The along-valley velocity scale in the upwelling regime, given by

$$V_u \approx \sqrt{\pi}\,\frac{H_c}{H_s}\frac{fW_c\lambda_{lw}}{2\pi L_x}\left(1+\frac{L_x^2}{L_c^2}\right)^{-1} e^{-(\pi W_c)/(\lambda_{lw})},$$

is based on potential vorticity (PV) conservation and lee-wave dynamics (H_s and H_c are the shelf and valley depth scales, respectively, and f is the Coriolis parameter). The velocity scale in the downwelling regime, given by

$$|V_d| \approx (H_c/H_s)[1+(L_x^2/L_c^2)]^{-1} fL_x,$$

is based on PV conservation. The velocity scales are validated by the numerical sensitivity simulations and can be useful for observational studies of along-valley transports. The work provides a framework for investigating cross-shelf transport induced by irregular shelf bathymetry and calls for future studies of this type under realistic environmental conditions and over a broader parameter space.

1. Introduction

Motivated by observations in the Hudson Shelf valley (HSV), this study aims to understand the dynamics controlling the cross-shelf (along valley) flow in an idealized shallow shelf valley. Observations in HSV show an asymmetrical flow response to winds of different directions: strong up-valley flow under eastward winds and much weaker down-valley flow under westward winds (Lentz et al. 2014). Numerical model simulations of an idealized shelf valley presented in Zhang and Lentz (2017, hereinafter Part I) describe a similar pattern of asymmetrical responses of the valley flow to along-shelf winds of opposite directions. When the wind forcing opposes the phase propagation of coastal-trapped waves (CTWs), referred to as the upwelling regime, a persistent, strong onshore upwelling flow is generated in the valley and occupies most of the valley cross section. When the wind forcing is in the same direction as the phase propagation of CTWs, referred to as the downwelling regime, the wind-driven along-shelf flow is deflected onshore over the eastern valley slope and then offshore over the western valley slope. This weak symmetric flow with respect to the valley axis results in a net offshore transport in the valley that is very weak compared to the onshore transport in the upwelling regime.

Corresponding author: Weifeng (Gordon) Zhang, wzhang@whoi.edu

DOI: 10.1175/JPO-D-17-0084.1

The analysis in Part I provides a physical explanation of the asymmetry between the upwelling and downwelling responses. In the upwelling regime the strong onshore flow results from the arrest of CTWs by the along-shelf flow and the generation of a coastal-trapped lee wave by the valley bathymetry. In the downwelling regime, the initial flow perturbation induced by the valley bathymetry radiates away from the source region because the shelf flow is in the same direction as CTW propagation and consequently does not trap CTWs.

One key property of the valley flows described in this study is the associated Rossby number:

$$\mathrm{Ro} = \frac{|U_s|}{fW_c}, \tag{1}$$

being $O(1)$. Here, U_s is the shelf velocity and defined here as the depth- and cross-shelf-averaged along-shelf velocity on the ambient shelf, f is the Coriolis parameter, and W_c is the valley width scale (see Table A1 in the appendix for the meaning of all notations used in this paper). The nonlinear momentum advection of the valley flow is thus important.

Previous studies have shown that the flow responses in deeper slope canyons to ambient along-isobath currents of opposite directions are also asymmetrical: strong up-canyon flow develops when the ambient current opposes the phase propagation of CTWs, and the flow tends to follow isobaths with weak offshore transport when the along-slope current aligns with the CTW propagation (e.g., Allen and Durrieu de Madron 2009; Kämpf 2006; Klinck 1996; She and Klinck 2000). Because of the similarities of the canyon physical setup to the shelf valleys, the mechanism of CTWs being arrested at the bathymetric perturbation and inducing persistent onshore flow is expected to be applicable to slope canyons.

There are also differences between slope canyons and shelf valleys. One aspect is their different depth H_c, which causes the influence of stratification to be different, as reflected in the Burger number:

$$S = \frac{NH_c}{fW_c} \tag{2}$$

Here, N is the buoyancy frequency. The S in deep slope canyons is often large, and stratification likely plays a major role in determining the canyon flow. The opposite is true for shallow shelf valleys.

Valleys and canyons provide important pathways of exchanging materials across continental shelves or between continental shelves and the open ocean (e.g., Bosley et al. 2004; Connolly and Hickey 2014; Crockett et al. 2008; Harris et al. 2003; Hickey et al. 1986; Michels et al. 2003; Williams et al. 2006). It is important to estimate the bathymetrically induced cross-shelf transport. Based on scaling of the momentum balance, Allen and Hickey (2010) provided a scale of the onshore transport of the subsurface offshore water in a slope canyon in the upwelling regime:

$$Q_u = \frac{f^{1/2} U_{\mathrm{sc}}^{3/2} W_{\mathrm{sc}} L_{\mathrm{sc}}^{1/2}}{N} F^{3/2}. \tag{3}$$

Here, U_{sc} is the along-slope velocity upstream of the canyon; W_{sc} is the width of the canyon at the shelf break; L_{sc} is the length of the canyon (in the cross-slope direction); $F = c_1 \mathrm{Ro}_r/(c_2 + \mathrm{Ro}_r)$, $\mathrm{Ro}_r = U_{\mathrm{sc}}/(fR_c)$ is the Rossby number defined based on R_c, the radius of curvature of the shelfbreak isobath at the upstream corner of the canyon; and c_1 and c_2 are empirical constants of order one.

Kämpf (2007) examined the parameter dependence of the up-canyon transport in the upwelling regime in numerical simulations and empirically obtained a scale of the transport:

$$Q_u = a \frac{f}{f_0} \frac{U_{\mathrm{sc}}^2 H_{\mathrm{sc}}}{N}, \tag{4}$$

where H_{sc} is the canyon depth relative to the shelf, and both f_0 and a are constants with empirical values obtained from the sensitivity simulations as $f_0 = 1.4 \times 10^{-4}\,\mathrm{s}^{-1}$ and $a \approx 32$.

Equations (3) and (4) depict different parameter dependences, except for the dependence on N. The transport in both formulas depends on N^{-1}, implying infinite onshore transport at the extreme condition of $N = 0$. This is not a major issue for their application in slope canyons, as the water column in deep canyons is always stratified. However, stratification in shallow shelf valleys can disappear at times. Any scaling that describes the along-valley transport would have to be able to accommodate the condition of no stratification.

A corresponding systematic quantification of the along-canyon transport in the downwelling regime is lacking, as fewer studies exist on the topic. The few existing studies examine the general influence of winds, stratification, and flow characteristics, as represented by Rossby and Burger numbers, on the along-canyon transport (e.g., Skliris et al. 2002; Spurgin and Allen 2014). Studies specifically on downwelling transport in slope canyons often focus on topographically induced dense water cascading (e.g., Chapman and Gawarkiewicz 1995; Wahlin 2002).

This paper, the second of two parts, examines the dynamics that control the strength of the along-valley flow in the respective upwelling and downwelling regimes using numerical model simulations of idealized shallow shelf valleys based roughly on HSV. Simplified vorticity and momentum balances of the valley flow and

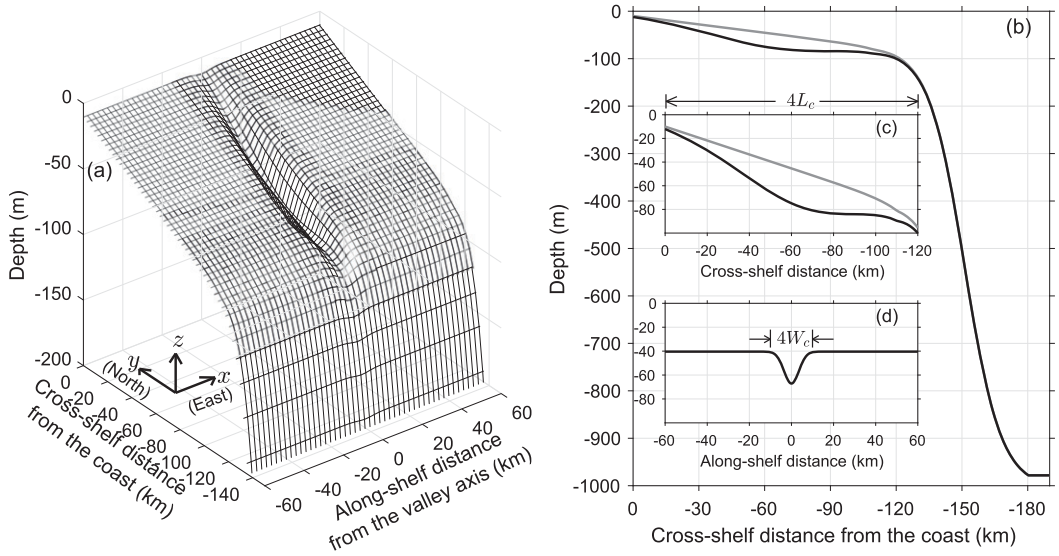

FIG. 1. (a) Model valley bathymetry in the control scenario; (b),(c) side-view of the bathymetry; (d) along-shelf section of the bathymetry at $y = -52$ km. The grid in (a) is 10 times coarser than the model grid in both x and y directions. The gray lines in (b) and (c) are the cross-shelf bathymetry outside of the valley, and the black lines are the cross-shelf bathymetry along the valley axis.

lee-wave dynamics are used to derive analytical scales of the cross-shelf flows and transports within the valley that are directly comparable to observations. The derived scales are compared to results of numerical simulations of the sensitivity to various parameters.

2. Numerical model

The regional ocean modeling system (ROMS; Shchepetkin and McWilliams 2008) is used in this study. The model solves the Boussinesq hydrostatic equations of motion and a density equation. It is set up in a Cartesian coordinate system with the positive x defined as eastward along shelf, positive y northward-pointing onshore, and positive z upward (Fig. 1). A rectangular model domain is used with edge lengths of 920 and 430 km in the x and y directions, respectively. The model bathymetry, given by

$$h_a = \max\left[0, \frac{h_f - h_c}{l_f}(l_f + y)\right] + h_p\left(\tanh\frac{y - y_p}{l_p} - 1\right) - h_f - H_c \exp\left[-\frac{(y - y_0)^2}{L_c^2} - \frac{(x - x_0)^2}{W_c^2}\right], \quad (5)$$

consists of an idealized shelf, slope, and a Gaussian-shaped shelf valley located at the along-shelf midpoint of the model domain. Here, $h_c = 10$ m is the coastal depth at the northern boundary; $h_f = 75$ m is the shelf depth scale; $l_f = 110.3$ km is the shelf width scale; $y_p = -151.3$ km is the y coordinate of the center of the slope; $l_p = 16.5$ km is the slope width scale; $h_p = 465$ m is the slope depth scale; L_c, W_c, and H_c are the valley length (cross-shelf direction), width (along-shelf direction), and depth scales, respectively; and $x_0 = 0$ and $y_0 = -65.3$ km are the coordinates of the valley center. Control values of the parameters are chosen to mimic the shelf, slope, and valley bathymetry around HSV. To remove ambiguity, we define the edge of the valley where the depth drop relative to the undisturbed shelf is $0.02H_c$. The total width of the valley is thus (Fig. 1d)

$$W_T \approx 4W_c. \quad (6)$$

The model domain is discretized into horizontal rectangular grids. The grid spacing in a central area of 160 km $\times$180 km that covers the valley is 250 and 300 m in the along- and cross-shelf direction, respectively, and it gradually increases outward reaching 3 km on the boundaries. In the vertical, the model employs a terrain-following grid with 80 layers. A closed wall condition is used on the northern boundary. The other three lateral boundaries are open with Chapman (1985), Flather (1976), and zero-gradient conditions for surface elevation, barotropic velocity, and baroclinic variables, respectively. A 100-km-thick wave-absorbing sponge layer is employed on all open boundaries. No explicit horizontal viscosity or diffusivity is used in the interior domain.

The model is initialized with horizontally uniform stratification of a constant buoyancy frequency N in the surface 200 m and $N = 0.001\,\mathrm{s}^{-1}$ below that. In the control cases, $N = 0.01\,\mathrm{s}^{-1}$ in the surface 200 m; steady uniform along-shelf wind stress of $\tau_s = \pm 0.2\,\mathrm{N\,m}^{-2}$ is applied on the surface for the upwelling and downwelling simulations, respectively; and quadratic bottom drag is applied with a coefficient $C_d = 0.003$. There is no surface or bottom buoyancy flux. The simulations all start from zero flow and are run for 10 days. The resolved shelf flow reaches a quasi-equilibrium state at Day 5 (see Fig. 7 in Part I). While the stratification continues evolving slowly after day 5, it does not significantly affect the shelf and valley flow (see below).

Sensitivity simulations for both the upwelling and downwelling regimes are conducted to examine the dependence of the along-valley flow on eight parameters: wind direction, along-shelf wind stress τ_s, f, N, W_c, H_c, L_c, and C_d. As this study focuses on shelf valleys geometrically similar to HSV, influences of other parameters (e.g., shelf depth and shelf slope) are not considered. Results of the sensitivity simulations provide guidance for developing and validating the dynamical scalings. In each simulation series, the value of one parameter is altered while all other parameters are fixed at the control values (see Table 1 in Part I for a complete list of model runs including the Burger and Rossby numbers for each run). We conducted two additional simulations with no bottom friction and $\tau_s = \pm 0.1\,\mathrm{N\,m}^{-2}$ to examine the valley responses to shelf flows of different strengths (see Part I). There are a total of 84 simulations with 42 in each flow regime described in this part of the study.

3. Parameter space and sensitivity

a. Parameter space

This study focuses on midlatitude cross-shelf-oriented valleys similar to HSV; that is, $H_c \approx O(10)$ m, $L_c \approx O(10)$ km, $W_c \approx O(1\text{–}10)$ km, and $f \approx O(10^{-5}\text{–}10^{-4})\,\mathrm{s}^{-1}$. The valleys are long in the cross-shelf direction with the cross- to along-shelf aspect ratio greater than 1 (i.e., $L_c > W_c$). Because N on a continental shelf is generally $O(10^{-2})\,\mathrm{s}^{-1}$ or less, the Burger number S of the valley flow is not large. In the control case, $f = 9.37 \times 10^{-5}\,\mathrm{s}^{-1}$, $H_c = 30$ m, $W_c = 5$ km, $N = 10^{-2}\,\mathrm{s}^{-1}$, and the initial $S \approx 0.64$. The sensitivity simulations together cover a Burger number range of 0 to 2, and in most of the simulations (72 out of the 84) the initial S is less than 1. As the ROMS simulations proceed, mixing gradually reduces N, which reaches about 80% of its initial value at day 3. Thus, S decreases slightly over the simulation period. The small to moderate S indicates that the vertical scale of the valley influence is similar to or greater than the total water depth and that the valley width is large compared to the internal Rossby radius. Specifically, (2) and (6) together imply that the total width of the valley is about 4 times of the baroclinic Rossby radius when $S = 1$. Thus, the valleys considered in this study are generally shallow, meaning that the shelf flow stretches to the full depth of the valley and the valley response is largely barotropic. It also means that the effect of rotation is strong and the influence of stratification is weak, which are consistent with the results of the sensitivity simulations (see below). Note that the moderate decrease of the Burger number in the first several days of the simulations owing to the temporal variation of the model stratification (Figs. 4 and 5 in Part I) does not change the dynamical regime.

The shelf velocity is normally $O(0.1)\,\mathrm{m\,s}^{-1}$, so the Rossby number of the valley flow Ro is generally $O(1)$. At the equilibrium state of the control simulations, $|U_s| \approx 0.45\,\mathrm{m\,s}^{-1}$ and Ro ≈ 1. The range of Rossby number covered by the sensitivity simulations is between 0.24 and 3.25. Consequently, the nonlinear momentum advection of the valley flow is important, and the valley width is the same order of magnitude as the advection length scale. Here, because the Coriolis force plays a primary role (see below), we assume that f^{-1} is the time scale of the valley flow and that the inertial length scale $|U_s|/f$, over which the flow feels the rotation, also represents the length scale associated with the momentum advection.

b. Dependence of valley flow on wind direction

Winds in reality are often in directions oblique to the along-shelf direction, which raises the issue of the relative contributions of the along- and cross-shelf components of the wind stress to the valley flow. To examine the dependence of the valley flow on wind direction, we analyze two sets of simulations. The first set consists of 12 simulations that are forced by wind stress of the same strength, $0.2\,\mathrm{N\,m}^{-2}$, but in different directions that are 30° apart. The 12 simulations thus cover the entire 360° range of wind direction. Wind direction in this study is defined as the direction winds blow toward, and wind angle is defined as the degree of clockwise rotation from north. The second set of simulations is forced by only the along-shelf component of wind stress with different strengths.

Comparison within the first set of simulations shows that valley flows driven by along-shelf winds are much stronger than those driven by cross-shelf winds. The velocity field at $z = -25$ m and $t = 3$ days from the simulations forced by cross-shelf (northward or southward) wind stress of $0.2\,\mathrm{N\,m}^{-2}$ (Figs. 2a,c) show very weak flows of less than $0.1\,\mathrm{m\,s}^{-1}$ both on the shelf and in the valley. In contrast, simulations forced by along-shelf

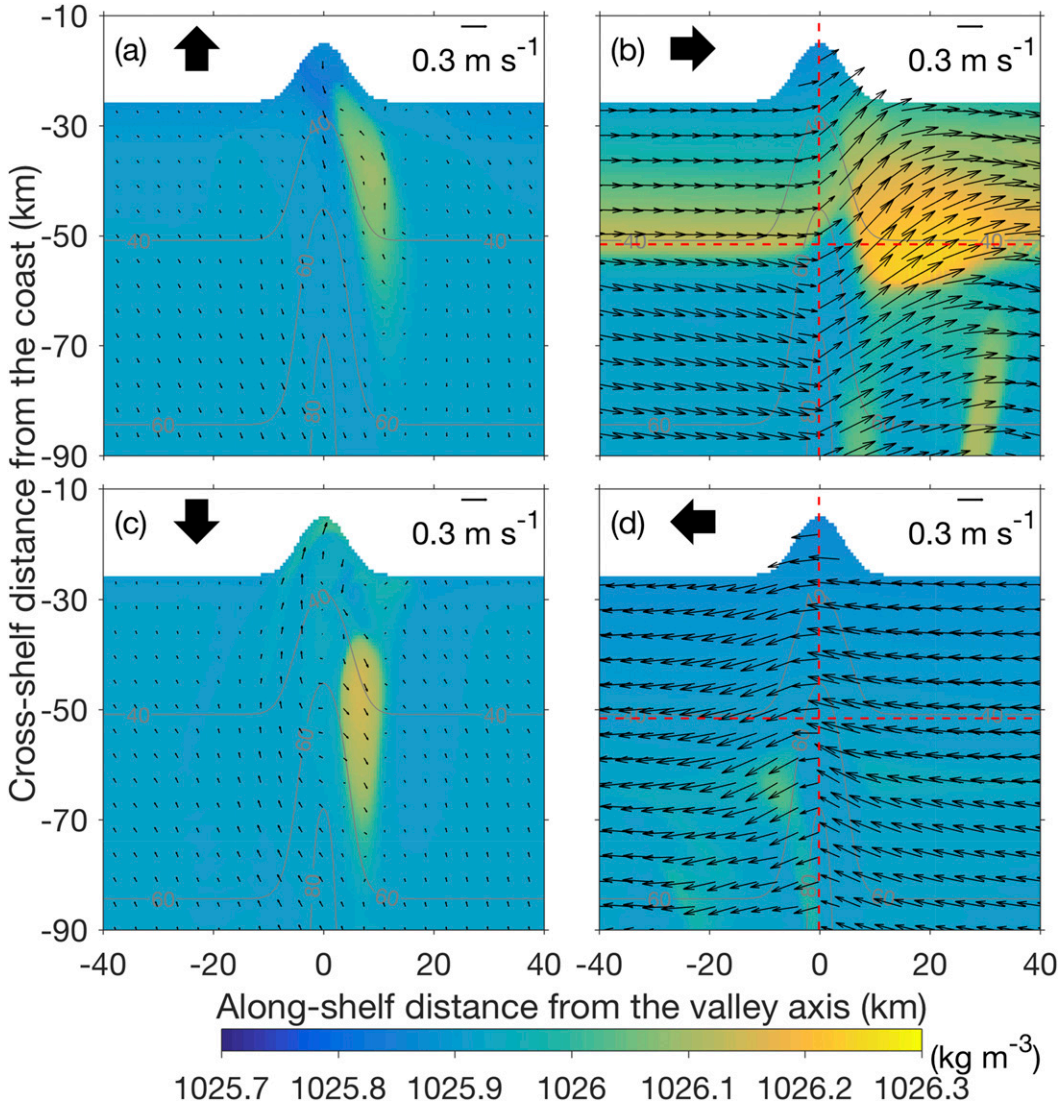

FIG. 2. Density (color) and horizontal velocity (arrows) at $z = -25$ m and $t = 3$ days from simulations forced by wind stress of the same strength but in different directions. The thick arrow at the top-left corner of each panel indicates the direction of the wind forcing, and the gray lines are isobath contours. The velocity scale is given at the top-right corner of each panel.

(westward or eastward) wind stress (Figs. 2b,d) show much stronger flow both on the shelf and in the valley. The maximum flow speed in the valley is greater than 0.5 m s^{-1}. The dependence on the wind direction of the depth-averaged along-valley velocity at $x = 0$ (on the valley axis) and $y = -52$ km (triangles in Fig. 3a) shows three groups: (i) for simulations forced by winds with an eastward component (30° to 150°N) the up-valley velocity is about 0.2 m s^{-1}; (ii) for simulations forced by winds with a westward component (−150° to −30°N) the down-valley velocity is <0.05 m s^{-1}; (iii) for simulations forced by northward (0°N) or southward (−180°N) wind the along-valley velocity is negligible. The difference between the first two groups is consistent with the asymmetrical response of valley flow to along-shelf winds of opposite directions examined in Part I. The along-valley volume transport over the valley cross section ($-2W_c < x < 2W_c$, at $y = -52$ km) depicts a very similar pattern (triangles in Fig. 3c).

Comparison between the two sets of simulations confirms that the along-shelf component of the wind stress predominantly determines the along-valley flow. When plotted against the along-shelf component of the wind stress, the along-valley velocity and transport from the two sets of simulations collapse (Figs. 3b,d), meaning that the contribution of the cross-shelf component of the

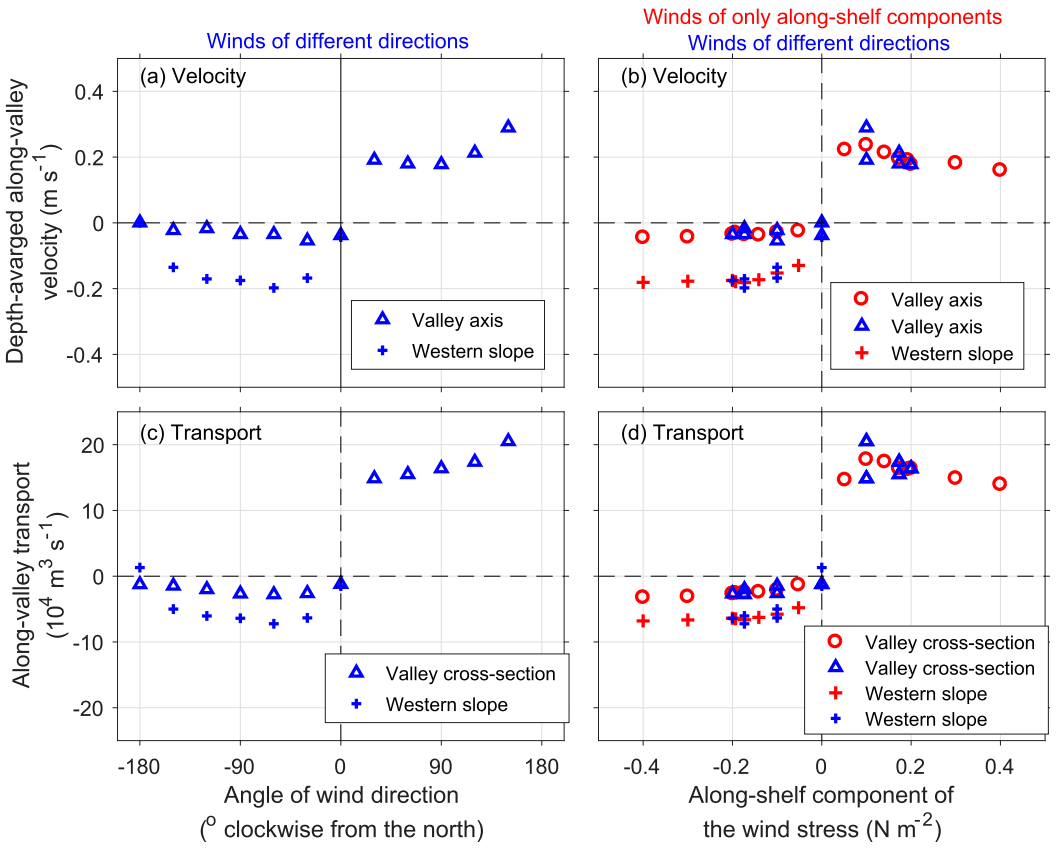

FIG. 3. Variations of depth-averaged (top) along-valley velocity and (bottom) along-valley transport at $y = -52$ km with respect to (left) wind direction and (right) along-shelf component of the wind stress at day 3. The blue symbols in both columns represent simulations forced by wind stress of the same strength ($0.2\,\mathrm{N\,m^{-2}}$) but in different directions; the red symbols represent simulations forced by only along-shelf wind stress of different strength. The triangles and circles represent (top) depth-averaged along-valley velocity on the valley axis and (bottom) along-valley transport averaged over the entire valley cross-section; the pluses represent (top) maximum down-valley velocity on the western valley slope and (bottom) along-valley transport averaged over the western half of the valley cross-section in the downwelling simulations.

wind stress to the valley flow is negligible. Hereby, we neglect the influence of cross-shelf winds in this paper, and the subsequent analysis focuses only on the valley response to along-shelf winds.

As described in Part I, the valley flow in the downwelling simulations forced by westward winds takes a shoreward detour over the valley with a largely symmetric pattern with respect to the valley axis (Fig. 2d). Because of the symmetry, the along-valley velocity averaged over the valley cross section, as indicated by the along-valley transport (triangles in Fig. 3c; also Fig. 8 in Part I), is generally very weak. This makes the analysis of cross-valley-averaged down-valley flow less meaningful. Observations in real valleys often capture velocity at particular sites rather than the cross-valley average. To make the result more relevant to observational studies, for the downwelling regime we choose to investigate the strength of the down-valley flow on the western slope of the valley, which is of similar strength as the up-valley flow on the eastern valley slope. Note that this down-valley flow on the western valley slope in the downwelling regime is not the counterpart of the up-valley flow in the upwelling regime that we investigate in this study. For completeness, the maximum down-valley velocity and the down-valley transport on the western slope of the valley in all downwelling simulations are also shown in Fig. 3 (pluses). They are also predominantly determined by the along-shelf component of the wind stress.

c. *Momentum balance*

The momentum balances in the control simulations confirm the importance of the nonlinear momentum advection. The dominant terms in the along-valley (cross shelf) momentum balance are the same in the upwelling and downwelling regimes. In both cases, the pressure gradient term is initially balanced by the

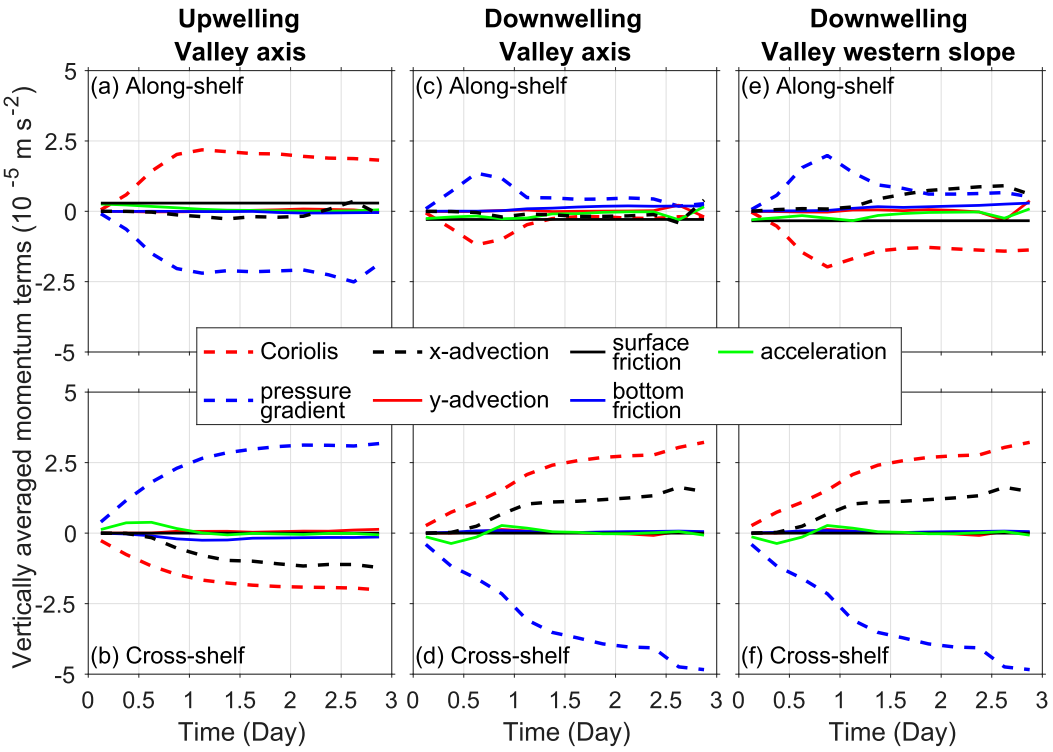

FIG. 4. Time series of vertically averaged (top) along- and (bottom) cross-shelf momentum terms at $y = -52$ km and on the valley (left; center) axis or (right) western slope from (left) upwelling and (center; right) downwelling simulations forced by eastward and westward winds, respectively.

Coriolis and acceleration terms and then, after ~1 day, by the Coriolis and cross-valley advection terms (Figs. 4b,d,f). The temporal evolution of the momentum balance indicates that, as the geostrophically balanced shelf flow initially enters the valley, the increased water depth causes the depth-averaged flow to slow down and results in a Coriolis force that is weaker than the along-valley pressure gradient force. The excessive along-valley pressure gradient force then drives a cross-shelf flow in the valley and creates the along-shelf gradient of the cross-shelf flow. The cross-valley advection term is associated with the cyclonic flow curvature over the valley in both regimes (Figs. 2b,d) and starts to increase at day 1. The cross-valley advection term eventually reaches about half the strength of the Coriolis term, contributing substantially to the momentum balance. Hence, the steady along-valley momentum balance is cyclostrophic in both upwelling and downwelling regimes: a balance among the Coriolis, cross-valley pressure gradient, and centrifugal force. The effect of the bottom friction on the along-valley momentum balance is negligible throughout the period in both regimes.

On the other hand, the cross-valley (along-shelf) momentum balances after the initial stage in the two regimes differ: *geostrophic* in the upwelling regime and *cyclostrophic* in the downwelling regime. In the upwelling case, it is largely geostrophic with the eastward Coriolis forcing balancing the westward pressure gradient force (Fig. 4a). Note that, consistent with the moderate S, the westward pressure gradient is mostly barotropic and caused by the upward sea level tilt toward the east associated with the arrested coastal-trapped lee wave (Part I). The contribution of the bottom friction remains negligible. The cross-valley momentum balance in the downwelling regime is more complex (Figs. 4c,e). It is largely geostrophic during the initial adjustment period of the first day. As the valley flow adjusts to the bathymetry and becomes symmetric with respect to the valley axis, both the eastward pressure gradient and westward Coriolis forces decrease substantially. On the valley axis where the down-valley flow is weak, the Coriolis term becomes similar in strength to the cross-valley advection and the wind stress, and all three terms together balance the eastward pressure gradient and bottom friction terms. On the western valley slope where the down-valley flow is relatively strong, the Coriolis term remains relatively large. Meanwhile, the cross-valley advection of the along-valley momentum increases with time and gradually exceeds the eastward pressure gradient force. The effect

of bottom friction increases over time but remains secondary at day 3. The cross-valley momentum balance on the western valley slope in the downwelling regime is thus largely cyclostrophic. Note that although the bottom friction is unimportant inside the valley, it is important on the ambient shelf and affects the valley circulation in both flow regimes through affecting the ambient shelf flow. The bottom drag coefficient is thus considered in the following sensitivity analysis.

d. Parameters dependence

The valley flow in both the upwelling and downwelling regimes varies with τ_s, f, N, W_c, H_c, L_c, and C_d (Fig. 5). The exact dependences of the along-valley velocity on the parameters differ in the two regimes. But the signs of the dependence of the along-valley speed on each of the parameters, except W_c, are the same for the two flow regimes. For instance, as f increases from 0.3×10^{-4} to $1.5 \times 10^{-4}\,\mathrm{s}^{-1}$, the modeled maximum depth-averaged up-valley velocity in the upwelling regime $V^m_{u,\max}$ increases from 0.12 to 0.5 m s^{-1}. For the same change of f, the maximum depth-averaged down-valley velocity in the downwelling regime $|V^m_{d,\min}|$ also increases but at a different rate, from 0.07 to 0.25 m s^{-1}. Similarly, both $V^m_{u,\max}$ and $|V^m_{d,\min}|$ increase with increasing H_c, increasing L_c, and decreasing C_d. The trends of $V^m_{u,\max}$ and $|V^m_{d,\min}|$ varying with W_c differ slightly. As W_c increases from 2.5 to 10 km, $V^m_{u,\max}$ increases from 0.22 to 0.44 m s^{-1}, and then $V^m_{u,\max}$ decreases to 0.35 m s^{-1} as W_c increases further to 20 km. Meanwhile, $|V^m_{d,\min}|$ increases monotonically with W_c, and it saturates for $W_c > 10$ km.

The different changing rates of $V^m_{u,\max}$ and $|V^m_{d,\min}|$ with respect to the parameters is presumably related to the differing cross-valley momentum balances in the two regimes: geostrophic in the upwelling regime and cyclostrophic in the downwelling regime (Fig. 4). But the consistency in the changing trends of $V^m_{u,\max}$ and $|V^m_{d,\min}|$ with respect to the parameters suggests that the underlying physical principle governing the valley flow in the upwelling versus downwelling regimes are similar. One likely underlying principle common for both regimes is the conservation of potential vorticity (PV). As the bottom friction is mostly negligible in both regimes, it is expected that PV is conserved over the valley. PV conservation is also consistent with the positive vorticity being generated when the shelf flow approaches the valley in both regimes, as described in Part I.

4. Analytical scaling

To understand the dependence of the valley flow on the parameters, scalings of the cross-shelf flow within the valley are derived for both the upwelling and downwelling flow regimes. Changes of the simulated along-valley velocity with respect to the parameters will be used to validate the scaling analyses.

The scaling analysis is based on five main assumptions: (i) geometrically long valley ($L_c > W_c$), (ii) equilibrium flow state, (iii) negligible bottom friction in the valley, (iv) shallow shelf valley with shelf flow stretching over the entire valley water column, (v) and negligible relative vorticity on the ambient shelf. The first assumption applies to shelf valleys that are geometrically similar to HSV. The second assumption will be discussed in detail in section 5. The third assumption is justified by the momentum balance analysis in section 3c, and the fourth assumption by the moderate Burger number considered here. The fifth assumption is generally valid because relative vorticity on the ambient shelf in both flow regimes, dominated by the cross-shelf shear of the along-shelf velocity (i.e., $\zeta_s \approx \partial U_s/\partial y$), is always small in magnitude. In the control case, $|\partial U_s/\partial y|$ on the ambient shelf is about $7 \times 10^{-7}\,\mathrm{s}^{-1}$, less than 1% of the inertial frequency f. Although it increases with wind stress, $|\partial U_s/\partial y|$ reaches only $3 \times 10^{-6}\,\mathrm{s}^{-1}$, ~3% of f, at the strongest wind stress ($\tau_s = 0.7\,\mathrm{N\,m}^{-2}$) used in this study.

With these assumptions, the PV conservation of the flow moving into the valley can be expressed as follows:

$$\frac{f}{H_s} = \frac{f + \zeta_c}{H_s + H_c}. \tag{7}$$

Here, H_s is the shelf depth scale; $\zeta_c = \partial V/\partial x - \partial U/\partial y$, the relative vorticity in the valley, is scaled as

$$\zeta_c \approx \frac{V}{L_x} - \frac{U}{L_y}; \tag{8}$$

U and V are scales of the depth-averaged velocity in the valley in the x and y direction, respectively; and L_x and L_y are the length scales of the valley flow in the x and y direction, respectively. Substituting (8) into (7) gives

$$\frac{fH_c}{H_s} \approx \frac{V}{L_x} - \frac{U}{L_y}. \tag{9}$$

From the continuity equation,

$$\frac{U}{L_x} + \frac{V}{L_y} \approx 0. \tag{10}$$

Combining (9) and (10) to get a scale for the along-valley flow gives

$$V \approx \frac{H_c}{H_s} f L_x \left(1 + \frac{L_x^2}{L_y^2}\right)^{-1}. \tag{11}$$

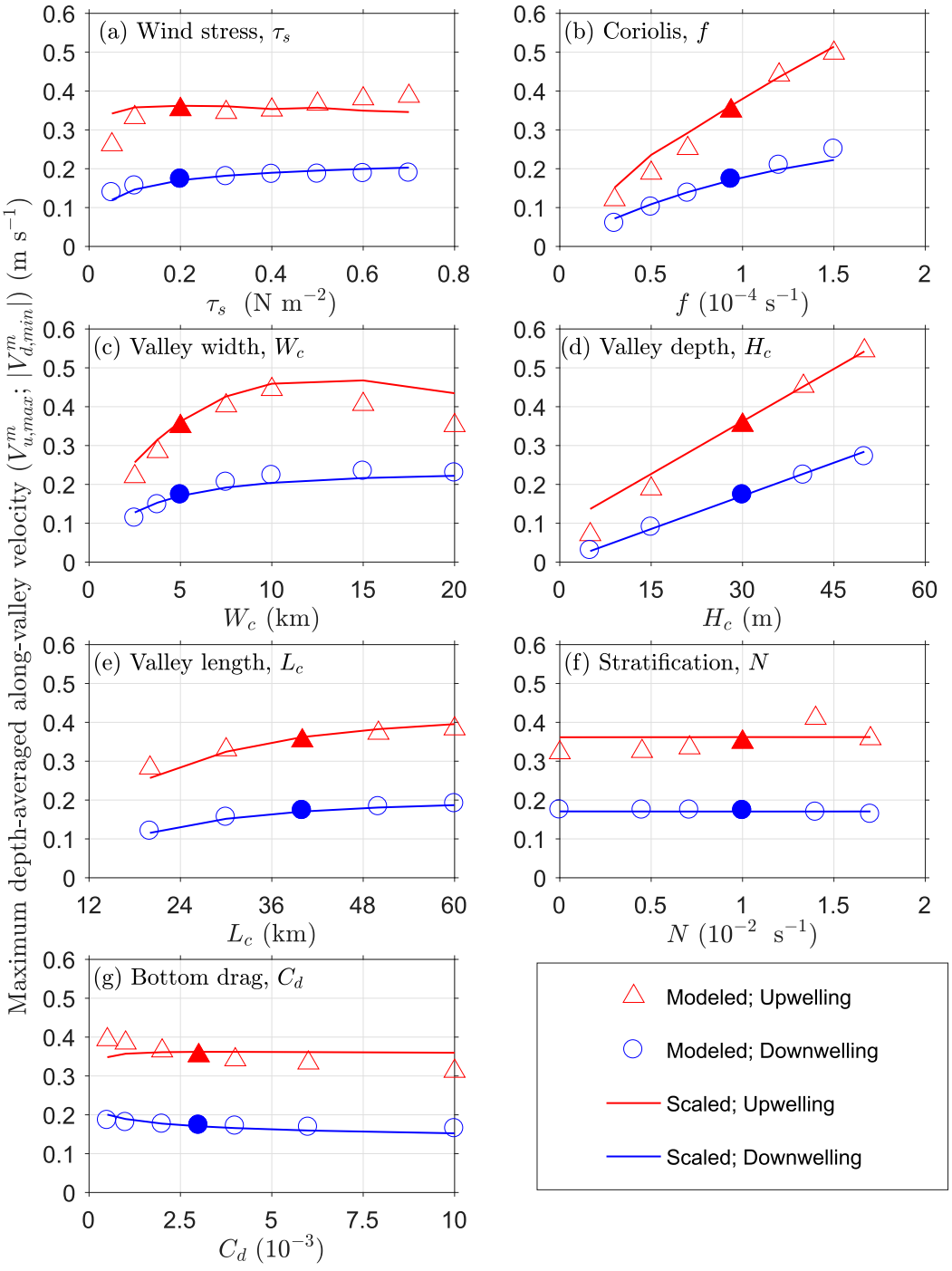

FIG. 5. Dependence of the modeled maximum depth-averaged up-valley and down-valley velocity on sensitivity parameters. The solid symbols represent the control simulations, and the red and blue solid lines represent the corresponding velocities given by the scalings in (17) and (22), respectively.

Note that when $H_c = 0$, (11) gives $V = 0$, satisfying the condition at the limit of no shelf valley.

To estimate the along-valley flow in (11), the appropriate length scales need to be determined. Because the cross-shelf bathymetry of the ambient shelf is fixed in this study, the shelf depth scale H_s does not vary. Here, it is chosen to be the shelf depth in (5); that is, $H_s = h_f = 75$ m. Note that using another constant value (e.g., $H_s = 48.5$ m, the shelf depth along the valley center) does not change the results present in this study. Because the

lengths of the valleys considered in this study are all smaller than the shelf width, the valley flows are constrained in the cross-shelf direction by the valley geometry. A natural choice of the cross-shelf length scale of the valley flow is the cross-shelf length scale of the valley bathymetry (i.e., $L_y = L_c$). There are three along-shelf length scales: 1) the valley width scale W_c, 2) the inertial length scale $|U_s|/f$, and 3) in the upwelling regime the wavelength of the lee wave $\lambda_{\rm lw}$. Because the flow responses in the shallow valleys studied here are largely barotropic with very small effect of stratification, the influence of baroclinic Rossby radius NH_c/f on the valley flow is presumably weak and neglected here. The $O(1)$ Ro implies that $|U_s|/f$ is on the same order of magnitude as W_c. That is, the along-shelf distance over which the flow starts to feel the rotation is close to the valley width. The L_x is likely determined by one of the three scales or some combination of them. Since the dynamics controlling the valley flow differs in the upwelling and downwelling regimes, L_x varies with the flow regime, which is discussed as follows.

a. Upwelling regime

Because the persistent valleywide up-valley flow under eastward wind is part of the onshore flow associated with the stationary coastal-trapped lee wave, the along-shelf length scale of the up-valley flow L_{xu} is associated with $\lambda_{\rm lw}$, the wavelength of the lee wave. As in Part I, $\lambda_{\rm lw}$ is estimated in this study as the along-shelf distance between the maximum and minimum of the SSH anomaly, which is obtained by subtracting the SSH to the far west of the valley. As described in Part I, $\lambda_{\rm lw}$ is determined by the intersection between the CTW dispersion curve and the line of $\omega = U_s k$ in the ω–k space. Here ω and k are frequency and wavenumber, respectively. Therefore, among the parameters considered in this study, the lee-wave wavelength $\lambda_{\rm lw}$ should depend on U_s, f, and N, but not on W_c, H_c, and L_c, because U_s, f, and N affect the CTW dispersion relationship or the $\omega = U_s k$ line, and the valley geometry does not. The $\lambda_{\rm lw}$ should also depend on τ_s and C_d because they affect U_s. The sensitivity simulations confirm these parameter dependences of the modeled lee-wave wavelength $\lambda_{\rm lw}^m$ (Fig. 6; also Fig. 13a in Part I). Note that the dependence of $\lambda_{\rm lw}^m$ on N is weak (Fig. 6g), presumably because the moderate Burger number limits the influence of the stratification.

Examination of the model runs indicates that L_{xu} also depends on W_c, especially in the cases of a wide valley with relatively small Ro (Fig. 10d in Part I). This is consistent with the dynamics at the limit of Ro $\ll 1$ with weak along-shelf flow or a wide valley. At this limit, the lee-wave response presumably becomes weak and $\lambda_{\rm lw}$ becomes relatively small, and the along-shelf length scale of the valley flow is determined by the other two length scales W_c and $|U_s|/f$. The W_c dominates the influence because Ro $\ll 1$ and $|U_s|/f \ll W_c$. This is also consistent with the combined along-shelf length scale of the valley flow in the downwelling regime when there is no lee wave (see section 4b). Therefore, a formulation of the along-shelf length scale of the up-valley flow in the upwelling regime should include the valley width influence at small Ro even though the flow is still controlled by the lee-wave response. A sensible definition of the along-shelf length scale is thus

$$L_{xu} = W_c + \lambda_{\rm lw}/8. \tag{12}$$

Here, the factor of 8 adjusts the lee wavelength scale to be consistent with W_c, which is a quarter of the valley width, as in (6).

A PV-based scaling of the up-valley flow in the upwelling regime is then from (11):

$$V_u = \frac{H_c}{H_s} f L_{xu} \left(1 + \frac{L_{xu}^2}{L_c^2}\right)^{-1}. \tag{13}$$

For validation, we substitute the corresponding parameter values and modeled lee-wave wavelength $\lambda_{\rm lw}^m$ into (12) and (13) and obtain a scaled up-valley velocity for each of the sensitivity simulations V_u. It is then compared to the maximum depth-averaged onshore velocity in the valley from the model $V_{u,\max}^m$ in both nondimensional and dimensional spaces (Figs. 7a,b). The nondimensionalization is achieved through normalizing V_u and $V_{u,\max}^m$ by U_s. Linear regressions applied to the scatterplots give linear fits with correlations significantly different from zero at the 95% confidence level (all fits shown in this work have correlation significantly different from zero at the 95% confidence level). The overall R^2 values of the velocity comparisons in the nondimensional and dimensional spaces are 0.9 and 0.76, respectively. However, (13) gives an increasing V_u with respect to W_c, which differs from the modeled $V_{u,\max}^m$, which decreases for $W_c > 10$ km (Fig. 5c). This discrepancy is likely caused by the fact that valley width is not directly included in the PV dynamics (it is included only indirectly in the formula through L_{xu}).

It is likely that the valley width also exerts direct influence on the up-valley flow through the establishment of the coastal-trapped lee wave, and this effect is not included in the PV-based derivation. To include it, we develop a scale of the onshore velocity within the valley based on the lee-wave dynamics following Martell and Allen (1979).

The amplitude of the lee wave depends on the projection of the bathymetric perturbation (the valley

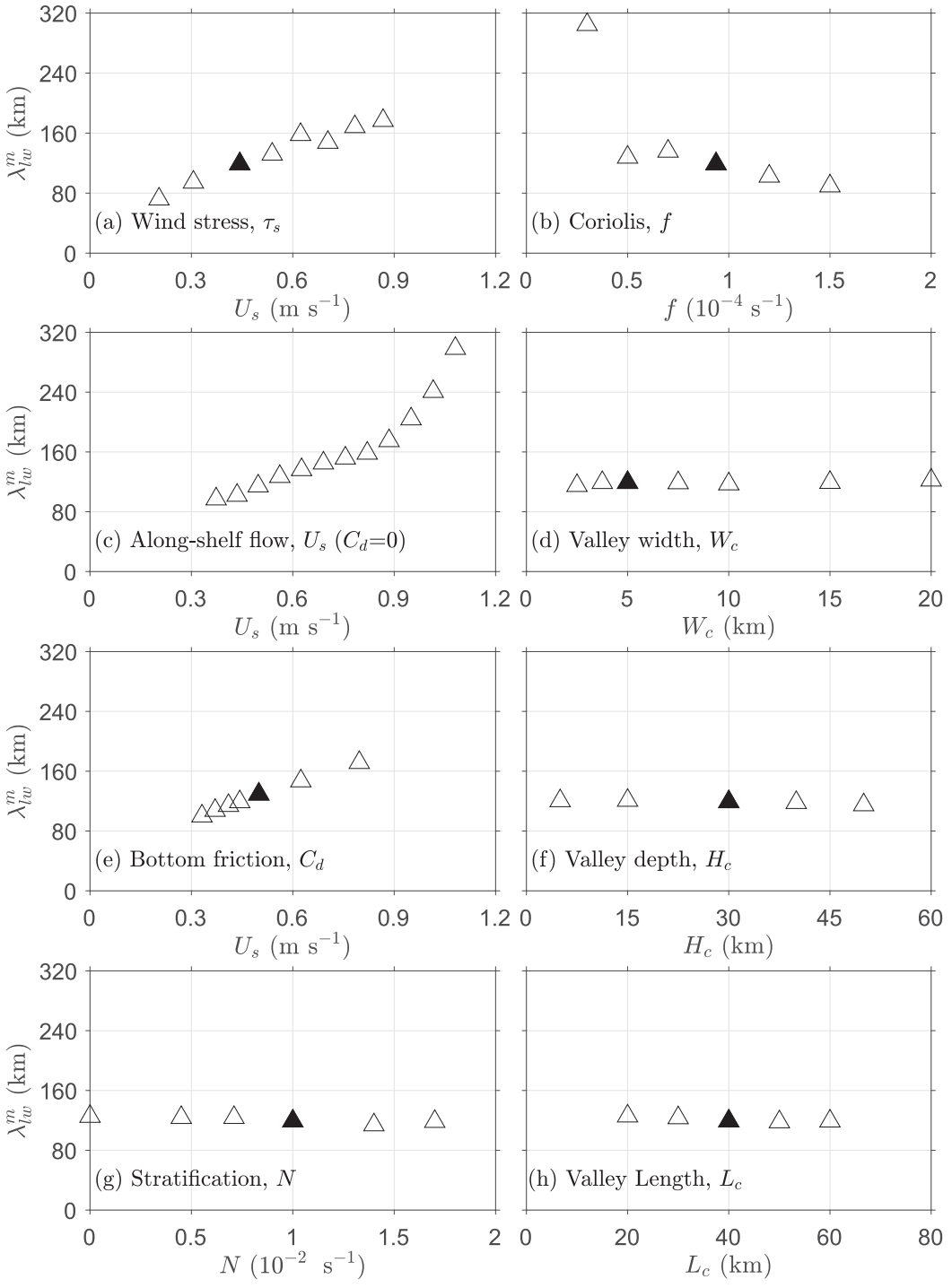

FIG. 6. Dependence of the wavelength of the coastal-trapped lee waves in the upwelling simulations (forced by eastward winds) on the model parameters. The solid symbols represent the upwelling control simulation.

in this case) on the lee-wave waveform (Baines 1995; Brink 1986; Martell and Allen 1979). The valley bathymetric variation in (5) in the along-shelf direction is a Gaussian function of x; that is, $h_x(x) = \exp[-(x - x_0)^2/W_c^2]$. The projection of this along-shelf bathymetric variation onto the lee-wave waveform is its Fourier transform (Abramowitz and Stegun 1965):

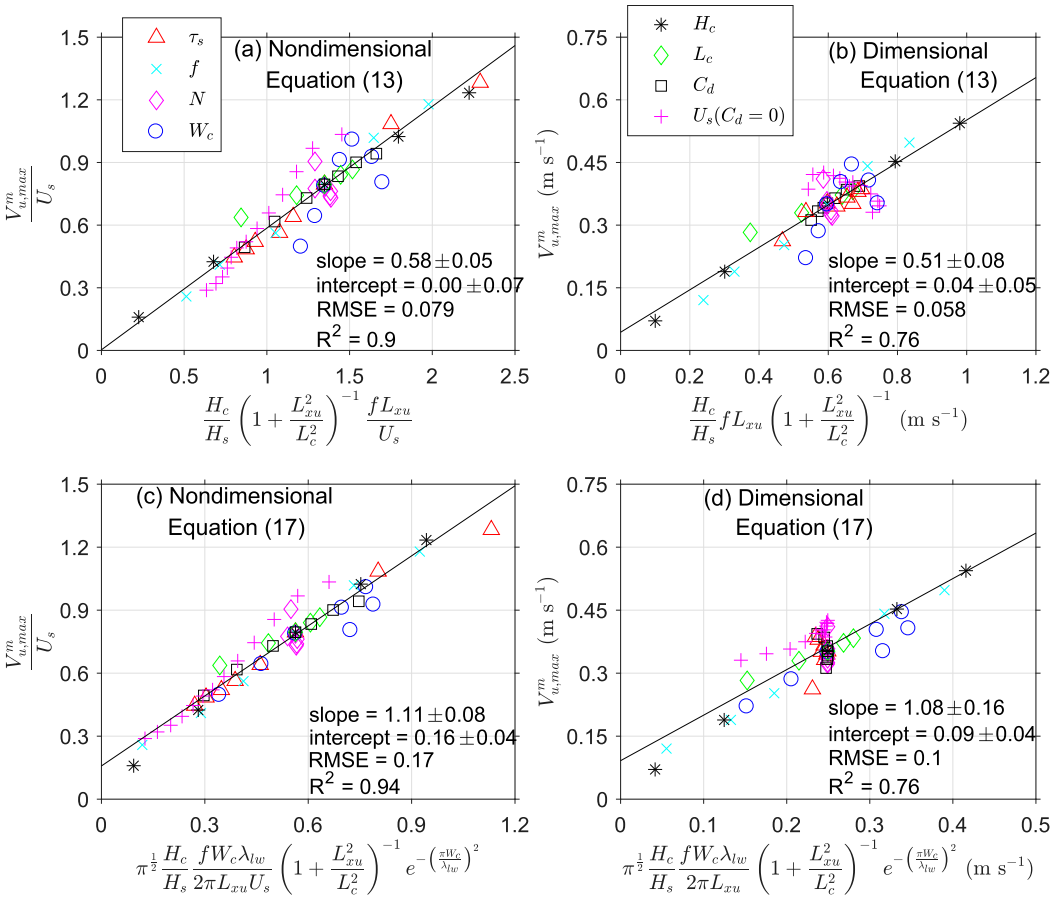

FIG. 7. Scatterplots of the maximum onshore velocity within the valley in the upwelling simulations vs scaled along-valley velocity in (left) nondimensional and (right) dimensional spaces. (top) The scaling is based only on potential vorticity conservation with the lee-wave wavelength incorporated [(13)]; (bottom) the scaling is based on both potential vorticity conservation and lee-wave dynamics and considers the influence of the valley bathymetric resonance [(17)]. Each type of symbol represents one sensitivity simulation series. The black lines are least squares fits with the corresponding slope, intercept, their respective 95% confidence intervals, root-mean-square error (RMSE), and R^2 given. Note that the legend is separated into two parts, and they together apply to all panels.

$$a_{\mathrm{lw}} = \int_{-\infty}^{\infty} e^{-(x-x_0)^2/W_c^2}\, e^{-i(2\pi x)/\lambda_{\mathrm{lw}}}\, dx = \sqrt{\pi} W_c\, e^{-[(\pi W_c)/\lambda_{\mathrm{lw}}]^2}. \tag{14}$$

This is essentially a resonant effect of the valley bathymetry. As the along-shelf length scale of the bathymetric perturbation gets close to the length scale of the lee wave, the lee-wave response strengthens. Following Martell and Allen (1979) for a barotropic CTW in a channel and (14), the scale for the sea level anomaly, which represents the intensity of the lee wave, can be expressed as follows:

$$\eta_u' \approx \sqrt{\pi} q \frac{H_c}{H_s} \frac{f^2 W_c \lambda_{\mathrm{lw}}}{2\pi g} e^{-[(\pi W_c)/\lambda_{\mathrm{lw}}]^2}. \tag{15}$$

Here, the nondimensional coefficient q represents the projection of the valley cross-shelf bathymetry onto the cross-shelf mode shape of the mode-2 CTW [see (2.14) in Martell and Allen (1979)]. Thus, q depends on the valley cross-shelf length scale L_c and the cross-shelf mode shape of the coastal-trapped lee wave, which depends on λ_{lw}. Similar to the argument in Part I about mode-2 CTWs dominating the lee-wave response, the efficiency of the cross-shelf bathymetric perturbation exciting mode-2 CTWs is determined by q. Because the CTW mode shape does not have an analytical formula, q cannot be derived analytically, as for a_{lw}. Here, we will seek to formulate q by considering the condition in wide valleys where lee-wave response is presumably weak and the effect of PV conservation presumably dominates. The along-valley velocity is obtained by assuming the along-valley flow is geostrophic and barotropic (Fig. 4a); that is, $V_u \approx \eta_u' g/(fL_{xu})$. The assumption of

geostrophy is consistent with the along-shelf momentum balance in the valley in the control simulation (Fig. 4a). This gives the onshore geostrophic velocity from (15):

$$V_u \approx \sqrt{\pi} q \frac{H_c}{H_s} \frac{f W_c \lambda_{\mathrm{lw}}}{2\pi L_{xu}} e^{-[(\pi W_c)/\lambda_{\mathrm{lw}}]^2}. \tag{16}$$

Considering a wide valley where the effect of PV conservation presumably dominates and following the expression in (13), we formulate the nondimensional coefficient, $q = (1 + L_{xu}^2/L_c^2)^{-1}$. Thus,

$$V_u \approx \sqrt{\pi}\, \frac{H_c}{H_s} \frac{f W_c \lambda_{\mathrm{lw}}}{2\pi L_{xu}} \left(1 + \frac{L_{xu}^2}{L_c^2}\right)^{-1} e^{-[(\pi W_c)/\lambda_{\mathrm{lw}}]^2}, \tag{17}$$

and

$$\eta_u' \approx \sqrt{\pi}\, \frac{H_c}{H_s} \frac{f^2 W_c \lambda_{\mathrm{lw}}}{2\pi g} \left(1 + \frac{L_{xu}^2}{L_c^2}\right)^{-1} e^{-[(\pi W_c)/\lambda_{\mathrm{lw}}]^2}. \tag{18}$$

Equations (17) and (18) essentially combine the PV conservation effect and the bathymetrical resonant effect. In particular, (17) is the product of (13), (14), as normalized by L_{xu}, and a length scale ratio $\lambda_{\mathrm{lw}}/(2\pi L_{xu})$. Because the along-shelf momentum balance in the upwelling regime is largely geostrophic, the SSH anomaly, as an indication of the intensity of the lee wave, is proportional to the overall onshore transport over half of the lee-wave wavelength. The corresponding scale for the along-valley transport inside the valley is given by

$$Q_u \approx \sqrt{\pi}\, \frac{H_c}{H_s} \frac{f W_c^2 (H_c + H_s) \lambda_{\mathrm{lw}}}{2\pi L_{xu}} \left(1 + \frac{L_{xu}^2}{L_c^2}\right)^{-1} e^{-[(\pi W_c)/\lambda_{\mathrm{lw}}]^2}. \tag{19}$$

The lee-wave-based scalings are validated by comparing the scaled and modeled quantities (Figs. 7–9). The modeled SSH anomaly of each sensitivity simulation is chosen to be the maximum SSH anomaly at $y = -52$ km, $\eta_{u,\max}'^{m}$ (see Fig. 10 in Part I). The scaled η_u' is obtained by substituting the corresponding parameter values and modeled lee-wave wavelength λ_{lw} into (12) and (18). The nondimensionalization is achieved through normalizing the modeled and scaled SSH anomaly by $fL_{xu}U_s/g$ (assuming $f \neq 0$ and $U_s \neq 0$). Figure 8 shows the collapse of all the SSH anomaly results around straight lines with relatively little scatter, indicating that (18) captures the dynamics controlling the SSH variability associated with the lee-wave development. As the intercepts of the least squares fits are very small, (18) satisfies the condition at the limits of $f \to 0$ or $U_s \to 0$ (i.e., $\lambda_{\mathrm{lw}} \to 0$).

Values of V_u given by (17) and modeled $V_{u,\max}^{m}$ of the sensitivity experiments align with each other very well in both nondimensional and dimensional spaces (Figs. 7c,d). The parameter dependences of the scaled V_u largely resemble the ROMS sensitivity runs (Fig. 5). In particular, similar to the ROMS result, the dependence of V_u on W_c changes signs at $W_c = 10$ km. This reverse of the trend reflects the bathymetric resonant effect, as the valley width increases from being smaller to being greater than the along-shelf length scale of the lee wave. The minor discrepancies in the dependences of V_u on τ_s, N, and C_d are presumably caused by the aforementioned assumptions employed in the scaling analysis.

The scaled transport given by (19) is compared to the modeled onshore transport averaged over the valley cross section at $y = -52$ km, along the center of the upstream anticyclonic flow anomaly (Part I). The comparison shows a collapse of the results around a straight line (Fig. 9), indicating the general validity of the scaled formula, which is essentially a modification of the PV-based scaling to include the effects of bathymetric lee-wave resonance. There is noticeable misalignment of the scaled and modeled transport, particularly for the simulations of varying valley length, which likely resulted from the computation of the modeled transport at a fixed cross-shelf location. In the model, there is onshore transport on the shelf to the east of the valley (Fig. 2 in Part I), which is about 1/3 of the onshore transport in the valley and varies slightly among the simulations. Note that the overall onshore transport associated with the lee wave is proportional to the SSH anomaly.

b. *Downwelling regime*

For the downwelling regime there are two along-shelf length scales to consider (since there is no lee wave), the valley width scale W_c and the inertial length scale $|U_s|/f$. Because of $O(1)$ Ro, they are of similar order of magnitude. Therefore, both are expected to play roles in the valley flow dynamics, and, presumably, the shorter one dominates. We combine them to form an along-shelf length scale of the downwelling valley flow as follows:

$$L_{xd} \approx c_0 \frac{(2\pi/4)(|U_s|/f) W_c}{W_c + (2\pi/4)|U_s|/f} \approx c_0 \frac{1}{1 + \pi \mathrm{Ro}/2} \frac{\pi}{2} \frac{|U_s|}{f}. \tag{20}$$

Here, c_0 is an empirical constant to be determined. We multiply $|U_s|/f$ by 2π to convert from radians to wavelength and then divide by 4 to make the length scale comparable to the valley width scale [$W_c \approx W_T/4$, as in (6)]. For small Ro, W_c is relatively large and (20) gives $L_{xd} \approx \pi|U_s|/2f$; for large Ro, W_c is relatively small, and (20) gives $L_{xd} \approx W_c$, satisfying the conditions at both limits.

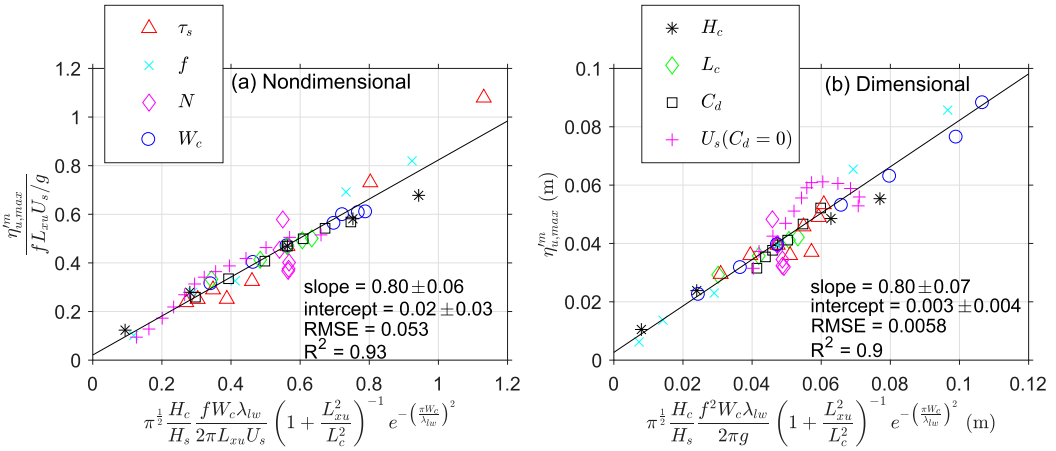

FIG. 8. Scatterplots of maximum SSH anomaly associated with the modeled coastal-trapped lee waves in the upwelling simulations vs scaled SSH anomaly in (left) nondimensional and (right) dimensional spaces. Each type of symbol represents one sensitivity simulation series. The black lines are least squares fits with the corresponding slope, intercept, their respective 95% confidence intervals, RMSE, and R^2 given in each panel.

To evaluate the scaling in (20) and associated parameter dependence, the modeled along-shelf length scale L_{xd}^m from each of the downwelling simulations is estimated from an along-shelf slice of the SSH anomaly induced by the valley bathymetry. The slice is from day 5 at $y = -52$ km. As described in Part I, $\eta_d'^m$ is defined as the difference between SSH everywhere and that at the same cross-shelf location and 200 km to the east of the valley (see Figs. 3d–f in Part I). A cosine function is fit to each of the along-shelf slices of $\eta_d'^m$, to obtain a wavelength λ_d^m (Fig. 10d). The fitting is based on $\eta_{d,\min}'^m$ and the along-shelf positions of $\eta_d'^m(x) = e^{-1}\eta_{d,\min}'^m$. To be consistent with the definition of W_c, we define

$$L_{xd}^m = \frac{\lambda_d^m}{4}. \tag{21}$$

Similar to the upwelling cases, the $\eta_d'^m$ and λ_d^m vary with the model parameters. For instance, the minimum SSH anomaly in the valley $\eta_{d,\min}'^m$ increases in magnitude with increasing τ_s, f, W_c (Figs. 10a–c), H_c, and L_c (not shown), and $\eta_{d,\min}'^m$ decreases in magnitude with increasing N and C_d (not shown). The λ_d^m varies strongly with U_s, τ_s, f, W_c, and C_d, but not with H_c, L_c, or N (Fig. 11). In particular, it increases with increasing $|U_s|$, increasing W_c, and decreasing f. The scaling in (20) is then evaluated by comparing the scaled length scale L_{xd}, with L_{xd}^m both normalized by $\pi|U_s|/2f$ in nondimensional space (Fig. 12a). The comparison shows a clear linear relationship between the modeled and scaled length scale with a slope $c_0 = 4.9$ and an intercept $b_0 = 0.38$. Applying c_0 and b_0 in the scaled wavelength gives a nearly one-to-one alignment with the modeled wavelength in the dimensional space (Figs. 11 and 12b). The comparisons indicate that (20) represents the along-shelf length scale of the sea level anomaly in the downwelling regime very well.

The scale of the along-valley flow in the downwelling regime is based only on the PV conservation [i.e., (11)] because there is no other mechanism controlling the valley flow. Replacing L_x in (11) with L_{xd} gives the formula for the scaled down-valley flow:

$$|V_d| \approx \frac{H_c}{H_s}\left(1 + \frac{L_{xd}^2}{L_c^2}\right)^{-1} fL_{xd}. \tag{22}$$

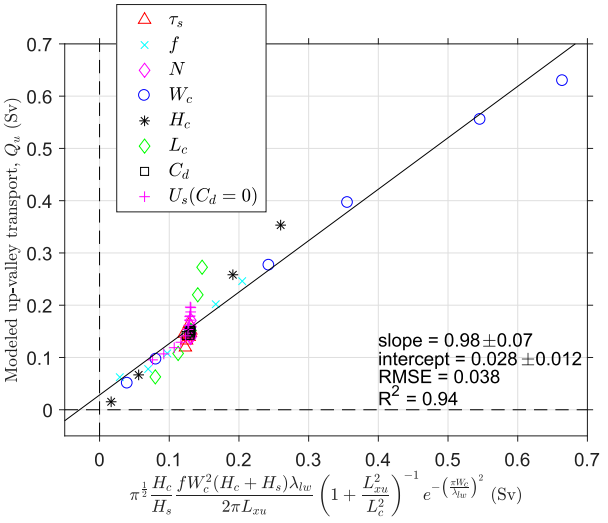

FIG. 9. A scatterplot of modeled vs scaled up-valley transport. The black line is a least squares fit with the corresponding slope, intercept, their respective 95% confidence intervals, RMSE, and R^2 given.

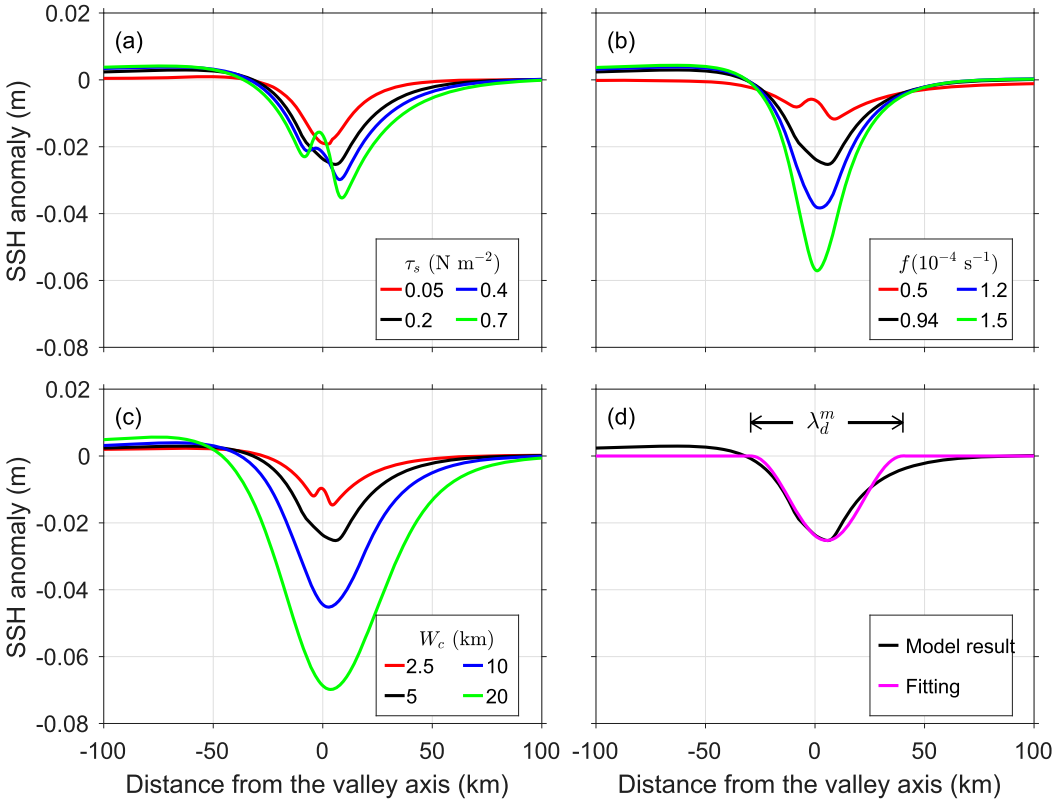

FIG. 10. Along-shelf section of the SSH anomaly $\eta_d'^m$ at $y = -52$ km and $t = 5$ days from downwelling simulations of different (a) wind strength, (b) Coriolis and (c) valley width, and (d) an example of a cosine curve (magenta line) over the valley with a wavelength of λ_d^m fitting the $\eta_d'^m$ curve. The black line in each panel is from the downwelling control simulation.

Here the effect of the valley width is embedded in L_{xd}. Note that (22) describes the down-valley flow on the western valley slope, not the net down-valley flow over the entire valley cross section. For validation, scaled along-valley velocity using (22) is compared to the minimum down-valley velocity (maximum speed) on the western slope of the valley $V_{d,\min}^m$ (Figs. 5 and 13). The general alignment of the results in both nondimensional and dimensional spaces indicates that the velocity scale in (22) agrees with the model result and that PV-based velocity scaling captures the dynamics of the valley detour flow in the downwelling regime.

As depicted in section 3c, the along-shelf momentum balance on the western valley slope in the downwelling regime is largely cyclostrophic, not geostrophic (Fig. 4e). For completeness, we nevertheless derive a scale of the SSH anomaly based on (22) and assuming the along-valley flow is geostrophic:

$$|\eta_d'| \approx \frac{f|V_d|L_{xd}}{g} = \frac{H_c}{H_s}\left(1 + \frac{L_{xd}^2}{L_c^2}\right)^{-1}\frac{f^2 L_{xd}^2}{g}. \qquad (23)$$

We do not expect (23) to represent the modeled SSH anomaly accurately. The scaled η_d' does not align with $\eta_{d,\min}'^m$ in the nondimensional space (Fig. 14a) as well as the velocity scaling (Fig. 13a), but the R^2 is 0.81. Interestingly, the comparison of η_d' and $\eta_{d,\min}'^m$ in dimensional space is better with the R^2 of 0.86 (Fig. 14b).

A scale of the down-valley transport on the western slope of the valley can then be derived based on (22):

$$|Q_d| \approx |V_d|(H_c + H_s)W_c = \frac{H_c(H_c + H_s)}{H_s}\left(1 + \frac{L_{xd}^2}{L_c^2}\right)^{-1} fW_c L_{xd}. \qquad (24)$$

The scaled along-valley transport generally aligns with the modeled down-valley transport on the western valley slope and the corresponding R^2 of 0.90 (Fig. 15). The minor discrepancies in the scaled versus modeled transport for H_c and W_c are likely related to the simple along-shelf and vertical length scales used in (24) to compute the transport from the velocity. Note that the discrepancies are much smaller in the dimensional

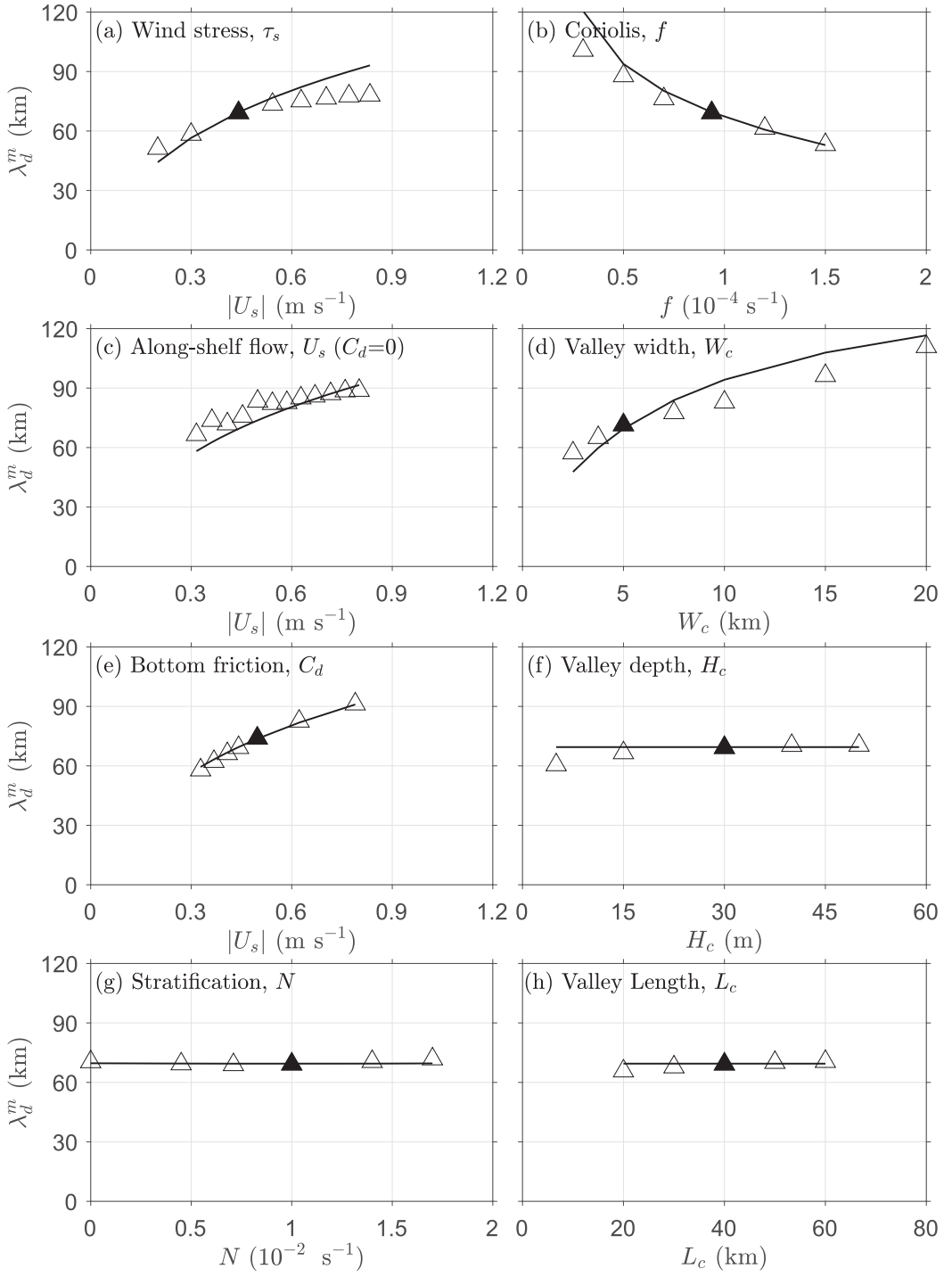

FIG. 11. Dependence of the wavelength of the onshore detour flow on the model parameters in the downwelling simulations. The solid symbols represent the downwelling control simulation, and the solid lines are the scaled wavelength based on (20) and (21).

velocity scaling (Fig. 13b). Equation (24) also provides a reasonable estimate of the up-valley transport on the eastern slope of the valley (not shown).

Overall, the scaling analysis presented here captures the main dynamics of the simulated onshore detour flow over the valley in the downwelling regime. The scaling

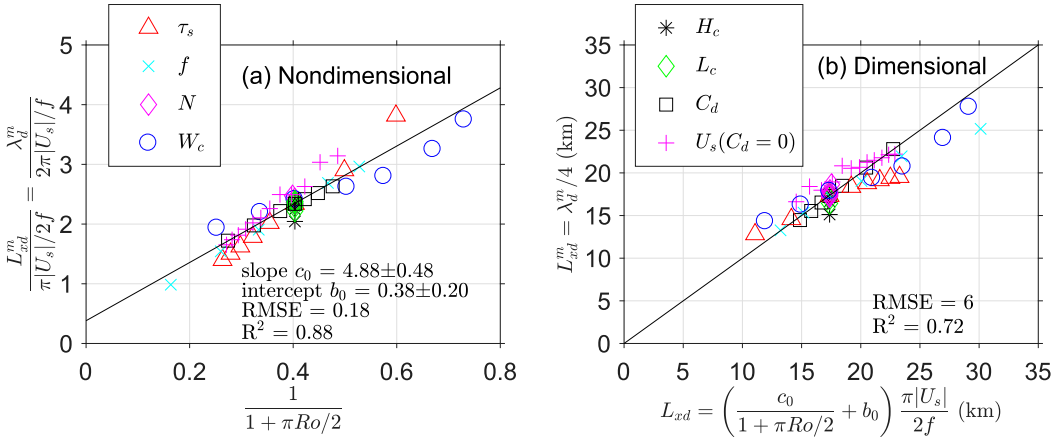

FIG. 12. Scatterplots of the along-shelf length scale of the valley flow detour in the downwelling simulations vs the scaled along-shelf length scale in (a) nondimensional and (b) dimensional spaces. Note that the slope c_0 and intercept b_0 in (a) are used in the dimensional length scale formula in (b). Each type of symbol represents one sensitivity simulation series. The black line in (a) is a least squares fit with corresponding slope, intercept, their respective 95% confidence intervals, RMSE, and R^2 given; the black line in (b) is a one-to-one diagonal line, and the corresponding RMSE and R^2 of the symbols relative to the diagonal line are also given.

analysis in this downwelling regime is based on PV conservation and the along-shelf length scale combining the valley width and the flow inertial length scale $|U_s|/f$.

5. Discussion

a. Comparison with other studies

The up-valley transport scale derived in this study, (22), cannot be directly compared to (3) and (4) for two reasons. First, the shallow valleys in this study occupy a different part of the parameter space than the slope canyons studied by Allen and Hickey (2010) and Kämpf (2007), particularly as characterized by S. Although the fundamental physics of arresting CTWs and generating persistent onshore flow should apply to slope canyons, the parameter dependence of the onshore flow is likely to differ because of the changes in the geometry and cross-shelf location of the bathymetrical perturbation. Second, (22) applies to the onshore transport over the entire valley water column, which is different from the onshore transport of offshore subsurface water considered in Allen and Hickey (2010) and Kämpf (2007). Because of the strong influence of stratification, the onshore transport in slope canyons is often confined to only a part of the water column. Both the Allen and Hickey (2010) and Kämpf (2007) studies treated the shelfbreak rim as a vertical separation and defined upwelling as the onshore motion of the offshore water below the shelfbreak rim. In a shallow shelf valley, the

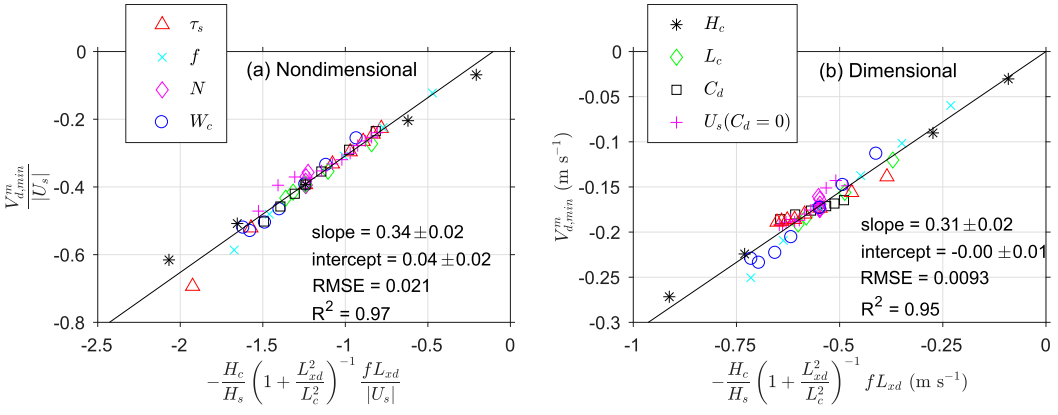

FIG. 13. Scatterplots of the maximum down-valley velocity in the downwelling simulations vs the scaled along-valley velocity in (a) nondimensional and (b) dimensional spaces. Each type of symbol represents one sensitivity simulation series. The black lines are least squares fits with the corresponding slope, intercept, their respective 95% confidence intervals, RMSE, and R^2 given in each panel.

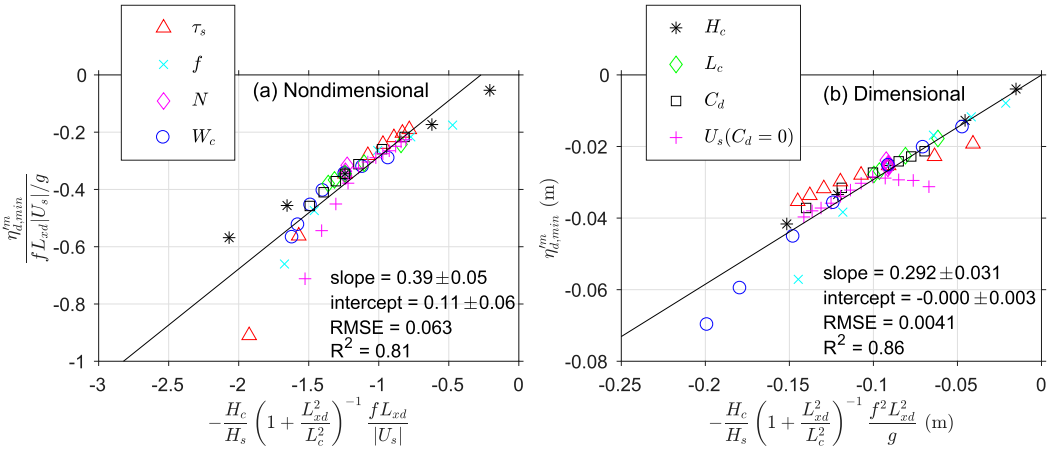

FIG. 14. Scatterplots of the minimum SSH anomaly in the valley resolved by the downwelling simulations vs the scaled SSH anomaly in (a) nondimensional and (b) dimensional spaces. Each type of symbol represents one sensitivity simulation series. The black lines are least squares fits with the corresponding slope, intercept, their respective 95% confidence intervals, RMSE, and R^2 given in each panel.

onshore motion spans the entire water column and there is no obvious separation in the vertical direction that can be used to divide the water column. A related aspect is the likely stronger influence of N in slope canyons, which may cause the baroclinic Rossby radius to be an important length scale in determining the canyon flow. Because of the weak influence of N in the shelf valleys considered here, the baroclinic Rossby radius does not play a major role, and its influence is not considered in the scaling analysis.

Nevertheless, one noticeable difference between (22) and (3) or (4) is in the application to an unstratified water column: (22) is perfectly applicable to unstratified conditions. The unstratified ROMS simulations give flow patterns and along-valley velocity similar to those in the corresponding control simulations (Figs. 5g,h), meaning the initial stratification does not substantially affect the depth-averaged valley flow in the cases studied here.

As discussed in Part I, the bathymetrical differences also cause the CTWs to be excited at slope canyons likely having different mode shape from those in shelf valleys. Therefore, (22) is unsuitable for slope canyons. This calls for numerical and observational studies of the canyon/valley flow over a broader parameter space. This work establishes a framework for such a study. However, as flow characteristics often vary with parameters, tackling the issue may require additional considerations, such as including the baroclinic Rossby radius as a length scale in determining the canyon flow.

b. *Applicability of scalings*

The scalings developed here are expected to be applicable to cross-shelf-oriented shelf valleys with geometric shape similar to the HSV and in the parameter space of $O(1)$ Ro, moderate (less than 2) S, and negligible bottom friction, as covered by the sensitivity simulations. However, the assumptions employed in the scaling analysis and the model simulations can also affect the applicability. While the exact influences of the assumptions remain to be investigated, we here discuss two issues related to the assumptions to point out specific topics for future studies.

First, this study assumes that the shelf flow is completely driven by the local wind and there is no background flow. In the real ocean, there are often background flows

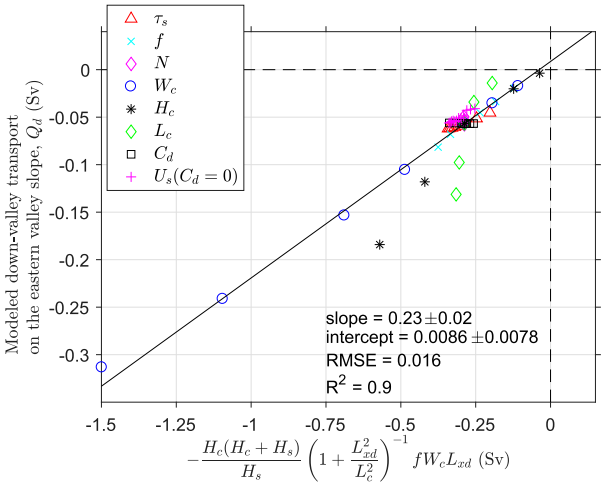

FIG. 15. A scatterplot of the down-valley transport on the eastern valley slope resolved by the downwelling simulations vs the scaled along-valley transport. The black line is a least squares fit with the corresponding slope, intercept, their respective 95% confidence intervals, RMSE, and R^2 given.

on continental shelves, driven by local buoyancy or offshore forcing. For instance, there is a persistent southwestward mean flow on the Mid-Atlantic Bight shelf (Lentz 2008a,b). It is obvious that the background shelf flow can also induce cross-shelf flow in a valley and modify the wind response. The fundamental mechanism leading to the asymmetrical valley flow should be the same whether the shelf flow is wind driven or is an ambient shelf flow forced by some other process. However, the background shelf flow may have a complex cross-shelf or vertical structure, which might alter the details of the valley response. For instance, if the mean flow is strongly sheared in the cross-shelf direction, the associated relative vorticity may break the assumption of weak background relative vorticity and modify the PV dynamics. Hence, the valley flow response to a background shelf flow will depend on the specific shelf condition, and how it modifies the wind response is a question that remains to be answered.

Second, vertically uniform stratification is used in the scaling analysis and model initial conditions. This is not expected to be a major issue for the shallow shelf valleys considered here because of the moderate S. In addition, vertical mixing quickly changes the vertical distribution of the model stratification and generates surface and bottom mixed layers similar to conditions on many shelves (Figs. 4–6 in Part I). Test simulations with vertically varying initial stratification (typical thermocline structure) give depth-averaged flow patterns very similar to the control simulations (not shown). However, the model results show that the vertical structure of the along-valley flow is sensitive to the stratification in the valley. In particular, the near-bottom intensification of the up- and down-valley flow, as observed in HSV (Lentz et al. 2014), is directly affected by the stratification in the valley. This will be the subject of a follow-up paper.

Last, this study focuses on the quasi-steady valley flow response rather than the initial transient response. In the control simulations, the adjustment to equilibrium takes 1–2 days (Fig. 4), and the valley responses to along-shelf flows in opposite directions are more symmetrical in the transient state. In particular, the simulation forced by westward wind gives a significant offshore flow on the valley axis in the first day (Fig. 7b in Part I). This is the flow response to the bathymetric perturbation before the initial disturbance radiates away. The increased water depth at the valley generates an excessive offshore pressure gradient force, which drives an initial offshore flow before the along-shelf advection term becomes significant (Fig. 4d). So in the real ocean, it is still possible to generate significant short-lived down-valley transport, for instance during sudden bursts of winds in the same direction as the CTW propagation. Because winds always fluctuate, it is necessary to consider this transient down-valley transport when studying the wind-driven cross-shelf exchange at a real shelf valley.

6. Summary

In this second part of the study, we focus on the wind-driven cross-shelf flow in shallow shelf valleys and the associated dynamics. The parameter space of interest is characterized by order-one Rossby number and small to moderate Burger number. Numerical simulations forced by winds of different directions show that the along-shelf component of the wind forcing dictates the flow response in the valley and that the contribution of the cross-shelf wind component is negligible. Consequently, the subsequent analysis focuses on the valley flow driven by along-shelf winds.

Part I of the study shows that the valley flow responds differently to the along-shelf winds of opposite directions. When the wind is in the direction opposite to the phase propagation of CTWs, a strong persistent onshore upwelling flow is generated in the valley as a result of CTWs being generated at the valley and then arrested by the shelf flow (i.e., a lee wave induced by the valley bathymetric perturbation). When the wind is in the same direction as the CTW phase propagation, the flow disturbance induced by the valley bathymetry propagates away, and the shelf flow adjusts to the bathymetry. The adjustment results in an up-valley flow on the eastern valley slope and a down-valley flow on the western slope. Together they form a symmetric flow pattern with a very weak offshore transport averaged over the valley cross section. In this paper, the dynamics that control the along-valley flow in both regimes are examined. The different valley flow responses to opposite along-shelf winds likely result in net up-valley transport of heat and salt and contribute to the cross-shelf heat and salt balance. To help quantify those, we develop scales for the along-valley flows and transports in each flow regime and compare them to results of the numerical sensitivity simulations.

In both flow regimes, potential vorticity (PV) conservation of the flow over the valley is assumed and used as the basis of the scaling analysis. The along-shelf length scale associated with the valley flow differs in the upwelling and downwelling regimes. In the upwelling regime, because the up-valley flow is influenced by the arrested CTWs, its along-shelf length scale is associated with the wavelength of the coastal-trapped lee wave. At the same time, the valley width scale W_c also affects the along-shelf length scale when $\mathrm{Ro} \ll 1$ and the lee-wave response is weak. In the downwelling regime, because the Rossby number of the valley flow is $O(1)$, W_c and the flow

TABLE A1. List of notations.

Variable	Meaning	First appearance
a	An empirical constant	(4)
a_{lw}	Fourier projection of the along-shelf bathymetric variation onto the lee-wave waveform	(14)
C_d	Coefficient of the quadratic bottom drag	Section 2
b_0	Intercept of the downwelling length scaling fitting	Section 4
c_0	Slope of the downwelling length scaling fitting	Section 4
c_1, c_2	Empirical constants	Section 1
c_r	Empirical constant	Section 4
F	An intermediate variable	(3)
f	Coriolis parameter	(1)
f_0	An empirical Coriolis constant	(4)
H_c	Valley depth relative to the neighboring shelf	(2)
H_s	Shelf depth scale	(7)
H_{sc}	Depth of a slope canyon	(4)
h_a	Model bathymetry	(5)
h_c	Depth on the coast	(5)
h_f	Shelf depth scale	(5)
h_p	Slope vertical scale	(5)
h_x	Along-shelf bathymetric variation of the valley	Section 4
k	Wavenumber	Section 4
L_c	Valley length scale in cross-shelf direction	(2)
L_{sc}	Cross-shelf length of a slope canyon	(3)
L_x, L_y	Length scales in the valley flow	(8)
L_{xd}	Along-shelf scale of the valley flow in the downwelling regime	(20)
L_{xd}^m	Modeled along-shelf scale of the valley flow in the downwelling regime	(21)
L_{xu}	Along-shelf scale of the valley flow in the upwelling regime	(8)
l_f	Shelf width scale	(5)
l_p	Slope width scale	(5)
N	Buoyancy frequency	(2)
q	A nondimensional coefficient describing the projection of the valley cross-shelf bathymetry onto the lee-wave mode shape	(15)
Q_u	Onshore volume transport within a shelf valley or canyon in the upwelling regime	(3)
Q_d	Offshore volume transport on the western valley slope in the downwelling regime	(20)
R_c	Radius of curvature of the shelfbreak isobath at the upstream corner of a slope canyon	Section 1
Ro	Rossby number of the valley flow	(1)
Ro_r	Rossby number of the canyon flow defined based on R_c	Section 1
(U, V)	Depth-averaged valley flow	(8)
U_s	Depth- and cross-shelf-averaged along-shelf flow	(1)
U_{sb}	Along-slope velocity	(3)
V_d	Scaled down-valley velocity in the downwelling regime	Section 4
$V_{d,\mathrm{min}}^m$	Modeled minimum down-valley velocity in the downwelling regime	Section 3b
V_u	Scaled up-valley velocity in the upwelling regime	Section 4
$V_{u,\mathrm{max}}^m$	Modeled maximum up-valley velocity (maximum speed) in the upwelling regime	Section 3b
W_c	Valley width scale in along-shelf direction	(1)
W_{sb}	Canyon width at the shelf break	(3)
W_T	The total width of the valley	Section 2
(x_0, y_0)	Coordinate of the valley center	(5)
y_p	y coordinate of the center of the slope	(5)
ζ_c	Relative vorticity of the valley flow	(7)
ζ_s	Relative vorticity of the ambient shelf flow	Section 4
η_d'	SSH anomaly in the downwelling regime	(23)
$\eta_d'^m$	Modeled SSH anomaly in the downwelling regime	Section 4
$\eta_{d,\mathrm{min}}'^m$	Modeled minimum SSH anomaly in the downwelling regime	Section 4
η_u'	SSH anomaly in the upwelling regime	(16)
$\eta_u'^m$	Modeled SSH anomaly in the upwelling regime	Section 4
$\eta_{u,\mathrm{max}}'^m$	Modeled maximum SSH anomaly in the upwelling regime	Section 4
λ_d	Along-shelf wavelength of the valley flow in the downwelling regime	Section 4
λ_d^m	Modeled along-shelf wavelength of the valley flow in the downwelling regime	Section 4
λ_{lw}	Along-shelf wavelength of the coastal-trapped lee wave	Section 4
λ_{lw}^m	Modeled along-shelf wavelength of the coastal-trapped lee wave	Section 4
τ_s	Surface wind stress	Section 2
ω	Wave frequency	Section 4

inertial length scale $|U_s|/f$ are the same order of magnitude. The along-shelf length scale of the valley flow is thus a combination of W_c and $|U_s|/f$. This difference in the flow length scales is one of the primary reasons that the along-valley flows in the upwelling and downwelling regimes are influenced by parameters in different ways.

In the upwelling regime, the up-valley flow is also affected by the lee-wave bathymetric resonance. Considering PV conservation and the lee-wave dynamics yields a scale of the onshore velocity within the valley [(17)] with good agreement with results of the sensitivity simulations. Scales of the up-valley transport and the SSH anomaly of the upstream meander are also derived, in (19) and (18), respectively.

In the downwelling regime, to be more relevant to observational studies, we consider the down-valley flow on the western slope of the valley, as the cross-valley-averaged down-valley flow is very weak. Combining W_c and $|U_s|/f$, we obtain an along-shelf length scale of the valley flow in (20), $L_{xd} = (1+\pi \mathrm{Ro}/2)^{-1}\pi|U_s|/2f$, and derive scales of the down-valley velocity and transport [(22) and (24)]. The sensitivity simulations validate the scaled formulas as they give values of the maximum down-valley velocity and down-valley transport aligning well with the scale estimates.

The analytical scalings presented here are based on several assumptions that may affect the applicability of the results. For instance, we neglect the background along-shelf flow that might modify the wind-driven valley response. The transient responses of the valley flow to the winds in the short initial stage are more symmetric with respect to the wind direction. This study also provides a framework for investigating cross-shelf flows induced by irregular shelf bathymetry over a broader parameter space. It is particularly important in future studies to include complex environmental conditions and to cover the ubiquitous slope canyons that occupy a different part of the parameter space than the shelf valleys considered in this study.

Acknowledgments. Both WGZ and SJL were supported by the National Science Foundation (NSF) through Grant OCE 1154575. WGZ is also supported by the NSF Grant OCE 1634965 and SJL by NSF Grant OCE 1558874.

APPENDIX

Notation

Table A1 provides a list of notations and their meanings and indicates where each first appears.

REFERENCES

Abramowitz, M., and I. A. Stegun, 1965: *Handbook of Mathematical Functions with Formulas, Graphs, and Mathematical Tables*. Dover Publications, 1046 pp.

Allen, S. E., and X. Durrieu de Madron, 2009: A review of the role of submarine canyons in deep-ocean exchange with the shelf. *Ocean Sci.*, **5**, 607–620, https://doi.org/10.5194/os-5-607-2009.

——, and B. M. Hickey, 2010: Dynamics of advection-driven upwelling over a shelf break submarine canyon. *J. Geophys. Res.*, **115**, C08018, https://doi.org/10.1029/2009JC005731.

Baines, P. G., 1995: *Topographic Effects in Stratified Flows*. Cambridge University Press, 482 pp.

Bosley, K. L., J. W. Lavelle, R. D. Brodeur, W. W. Wakefield, R. L. Emmett, E. T. Baker, and K. M. Rehmke, 2004: Biological and physical processes in and around Astoria submarine canyon, Oregon, USA. *J. Mar. Syst.*, **50**, 21–37, https://doi.org/10.1016/j.jmarsys.2003.06.006.

Brink, K. H., 1986: Topographic drag due to barotropic flow over the continental shelf and slope. *J. Phys. Oceanogr.*, **16**, 2150–2158, https://doi.org/10.1175/1520-0485(1986)016<2150:TDDTBF>2.0.CO;2.

Chapman, D. C., 1985: Numerical treatment of cross-shelf open boundaries in a barotropic ocean model. *J. Phys. Oceanogr.*, **15**, 1060–1075, https://doi.org/10.1175/1520-0485(1985)015<1060:NTOCSO>2.0.CO;2.

——, and G. Gawarkiewicz, 1995: Offshore transport of dense shelf water in the presence of a submarine canyon. *J. Geophys. Res.*, **100**, 13 373–13 387, https://doi.org/10.1029/95JC00890.

Connolly, T. P., and B. M. Hickey, 2014: Regional impact of submarine canyons during seasonal upwelling. *J. Geophys. Res. Oceans*, **119**, 953–975, https://doi.org/10.1002/2013JC009452.

Crockett, J. C., C. A. Nittrouer, A. S. Ogston, D. F. Naar, and T. T. Donahue, 2008: Morphology and filling of incised submarine valleys on the continental shelf near the mouth of the Fly River, Gulf of Papua. *J. Geophys. Res.*, **113**, F01S12, https://doi.org/10.1029/2006JF000674.

Flather, R. A., 1976: A tidal model of the northwest European continental shelf. *Mem. Soc. Roy. Sci. Liege*, **10**, 141–164.

Harris, C. K., B. Butman, and P. Traykovski, 2003: Winter-time circulation and sediment transport in the Hudson Shelf Valley. *Cont. Shelf Res.*, **23**, 801–820, https://doi.org/10.1016/S0278-4343(03)00025-6.

Hickey, B., E. Baker, and N. Kachel, 1986: Suspended particle movement in and around Quinault submarine canyon. *Mar. Geol.*, **71**, 35–83, https://doi.org/10.1016/0025-3227(86)90032-0.

Kämpf, J., 2006: Transient wind-driven upwelling in a submarine canyon: A process-oriented modeling study. *J. Geophys. Res.*, **111**, C11011, https://doi.org/10.1029/2006JC003497.

——, 2007: On the magnitude of upwelling fluxes in shelf-break canyons. *Cont. Shelf Res.*, **27**, 2211–2223, https://doi.org/10.1016/j.csr.2007.05.010.

Klinck, J. M., 1996: Circulation near submarine canyons: A modeling study. *J. Geophys. Res.*, **101**, 1211–1223, https://doi.org/10.1029/95JC02901.

Lentz, S. J., 2008a: Observations and a model of the mean circulation over the Middle Atlantic Bight continental shelf. *J. Phys. Oceanogr.*, **38**, 1203–1221, https://doi.org/10.1175/2007JPO3768.1.

——, 2008b: Seasonal variations in the circulation of the Middle Atlantic Bight continental shelf. *J. Phys. Oceanogr.*, **38**, 1486–1500, https://doi.org/10.1175/2007JPO3767.1.

——, B. Butman, and C. Harris, 2014: The vertical structure of the circulation and dynamics in Hudson Shelf valley. *J. Geophys. Res. Oceans*, **119**, 3694–3713, https://doi.org/10.1002/2014JC009883.

Martell, C. M., and J. S. Allen, 1979: The generation of continental shelf waves by alongshore variations in bottom topography. *J. Phys. Oceanogr.*, **9**, 696–711, https://doi.org/10.1175/1520-0485(1979)009<0696:TGOCSW>2.0.CO;2.

Michels, K. H., A. Suckow, M. Breitzke, H. R. Kudrass, and B. Kottke, 2003: Sediment transport in the shelf canyon ''Swatch of No Ground'' (Bay of Bengal). *Deep-Sea Res. II*, **50**, 1003–1022, https://doi.org/10.1016/S0967-0645(02)00617-3.

Shchepetkin, A. F., and J. C. McWilliams, 2008: Computational kernel algorithms for fine-scale, multiprocess, long-term oceanic simulations. *Handbook of Numerical Analysis XIV: Computational Methods for the Atmosphere and the Ocean*, P. G. Ciarlet, R. Temam, and J. Tribbia, Eds., Elsevier Science, 121–183.

She, J., and J. M. Klinck, 2000: Flow near submarine canyons driven by constant winds. *J. Geophys. Res.*, **105**, 28 671–28 694, https://doi.org/10.1029/2000JC900126.

Skliris, N., J. H. Hecq, and S. Djenidi, 2002: Water fluxes at an ocean margin in the presence of a submarine canyon. *J. Mar. Syst.*, **32**, 239–251, https://doi.org/10.1016/S0924-7963(02)00036-2.

Spurgin, J. M., and S. E. Allen, 2014: Flow dynamics around downwelling submarine canyons. *Ocean Sci.*, **10**, 799–819, https://doi.org/10.5194/os-10-799-2014.

Wahlin, A. K., 2002: Topographic steering of dense currents with application to submarine canyons. *Deep-Sea Res. I*, **49**, 305–320, https://doi.org/10.1016/S0967-0637(01)00058-9.

Williams, W. J., E. C. Carmack, K. Shimada, H. Melling, K. Aagaard, R. W. Macdonald, and R. G. Ingram, 2006: Joint effects of wind and ice motion in forcing upwelling in Mackenzie Trough, Beaufort Sea. *Cont. Shelf Res.*, **26**, 2352–2366, https://doi.org/10.1016/j.csr.2006.06.012.

Zhang, W., and S. J. Lentz, 2017: Wind-driven circulation in a shelf valley. Part I: Mechanism of the asymmetrical response to along-shelf winds in opposite directions. *J. Phys. Oceanogr.*, **47**, 2927–2947, https://doi.org/10.1175/JPO-D-17-0083.1.